NRIAG JOURNAL OF ASTRONOMY AND GEOPHYSICS
2024, VOL. 13, NO. 1, 182–206
https://doi.org/10.1080/20909977.2024.2413338

Taylor & Francis
Taylor & Francis Group

ARTICLE

OPEN ACCESS Check for updates

Utilising the 3D mineral system approach to identify the source of alluvial gold deposits in Ibala Town, Southwest Nigeria: an In-depth geological and geophysical exploration

Ifedayo Fadakinte

Research and Exploration Team, Energy and Mineral Resources Limited, Lagos, Nigeria

ABSTRACT

The Ibala gold field, discovered by artisanal miners in 2018, is located east of Ibala town in Osun State, southwest Nigeria. As older mines are depleted and abandoned, miners are now investigating the source of the deposits, believed to be auriferous quartz veins. This study uses the mineral system approach to trace the origin of the alluvial gold in the Ibala area. The research is conducted in three phases: first, a detailed analysis of the region's structural patterns and rock distribution is undertaken to understand the area's tectonic history. Next, a 3D conceptual model is created using an integrated geological and geophysical modeeling techinque to identify exploration targets and map the mineral system components. Finally, on-site verification is performed to validate the findings. The study reveals that the gold originates from auriferous shear zones characterized by high conductivity and chargeability geophysical signatures. These zones were formed by auriferous fluids released during the metamorphic devolatilization of deep volcanic rocks. As the fluids migrated through shear zones, they interacted with host rocks, precipitating gold alongside pyrite. When weathered, the gold-bearing material is transported via drainage channels, which miners now exploit. By using a mineral system approach, this research pinpoints the primary gold sources, supporting more efficient resource management and sustainable mining practices in the region.

ARTICLE HISTORY
Received 23 February 2024
Revised 18 August 2024
Accepted 1 October 2024

KEYWORDS
Ilesha gold exploration; 3D mineral system modelling; 3D geophysical exploration; 3D geological modelling; Orogenic gold

1. Introduction

The Ibala gold field is a group of alluvial mines discovered by artisanal miners in 2018. These mines are situated to the east of Ibala town in Osun State, southwest Nigeria (Figure 1). Gold extraction involves hand-dug trenches that extend to depths over 5 metres, and in certain locations, pits are dug vertically to about 12 metres (Figure 2). The local miners who discovered the alluvial gold lacked scientific knowledge regarding its mode of occurrence, mineralisation style, and primary source. Consequently, there is currently no established strategy for effectively and efficiently exploiting the gold resources in the area. Presently, alluvial gold production in the area is declining as the oldest mining pits have been fully exploited and abandoned. To revitalise gold production, artisanal miners are now focusing on locating the source of the alluvial gold deposits, which are believed to be auriferous quartz veins. However, these veins are often concealed beneath thick layers of overburden, presenting a challenge for gold prospectors. In such situations, the mineral systems approach becomes indispensable for gold exploration.

The mineral system approach to mineral exploration is a comprehensive framework that aims to understand all geological factors that control the generation and preservation of mineral resources (Wyborn et al. 1994). In the last decade, the mineral system approach has reached prominence as a critical method in mineral exploration and ore targeting (McCuaig et al. 2010; Witherly 2015; Hagemann et al. 2016; Huston et al. 2016; Wyman et al. 2016). The mineral system approach recognises that mineral deposits are the result of specific geological events and conditions. It considers the entire mineralisation process from the sources of metals and fluids to the deposition of metals in economically viable concentrations. The approach begins by identifying the key components of a mineral system, which typically include: (1) sources of mineralising fluids and ore-transporting ligands, (2) sources of metals and other ore components (3) migration pathways, (4) physical and chemical traps for metal, (5) preservation. Overall, the mineral system approach provides a conceptual framework to guide mineral exploration efforts, helping to increase the chances of discovering economically viable mineral resources while reducing exploration risks and costs.

This study seeks to determine the origin of alluvial gold deposits in the Ibala gold field through the mineral system approach. A 3D conceptual model was created using airborne geophysical data to identify

CONTACT Ifedayo Fadakinte Ifedayo.fadakinte@emrng.com Energy and Mineral Resources Limited, Research and Exploration Team,Lagos, Nigeria

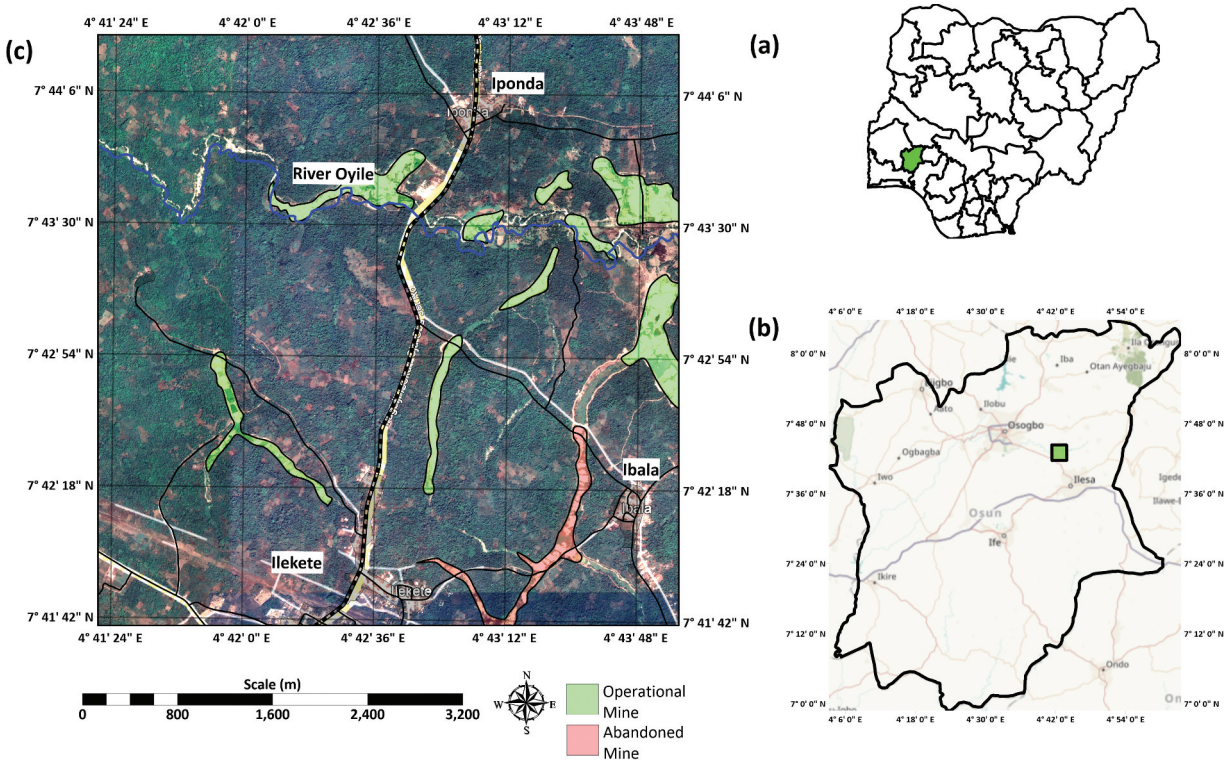

Figure 1. (a) The map of Nigeria showing Osun State highlighted in green. (b) The map of Osun State showing the location of the study area (green box). (c) The map of the study area showing the location of alluvial gold mines.

Figure 2. (a) photograph of alluvial gold mine. (b) gold panning by artisanal miners. (c) gold mining using hand dug trenches.

exploration targets, which were then verified through a ground-truthing exercise. By employing the mineral system approach, the study locates economically viable gold deposits, aiding in the planning, improvement, and sustainable management of gold resources in the local community.

1.1. Gold mineralization in Ilesha and its environs

Gold was first discovered in the region during the 1940s, and since then, it has become a significant contributor to Nigeria's annual gold production. The Ministry of Mines and Steel Development (MMSD) reports that alluvial gold mines in the area account for approximately half of the country's total gold output. In the 1980s, the defunct Nigerian Mining Corporation (NMC) conducted a reconnaissance geochemical study, revealing substantial alluvial gold resources in Itagunmodi, Osu, Ibode, and Oshu (Figure 3). The results of this survey indicated a spatial correlation between alluvial gold deposits and metavolcanic rocks. Elueze and Olade (1985) demonstrated that the alluvial gold deposits originated from the weathering of an interconnected network of auriferous quartz veins situated within meta-volcanic host rocks. The NMC also explored primary gold deposits in Ipetu and Iperindo, discovering gold within North-Northeast shear zones. Detailed microscopic analysis showed that sulphide grains frequently coexist with small gold specks (Oyinloye 2006).

Oyinloye and Steed (1996) demonstrated that the mineralising fluid originated from metamorphic processes and occurred at temperatures exceeding 286 degrees Celsius. Oyinloye (2006) postulated that the gold was leached from metavolcanic rocks by metamorphic fluids during the pan-African orogeny.

1.2. Regional geology

The regional geology of the study area is divided into three tectono-stratigraphic units namely: the Archean migmatite-gneisses complex; the Proterozoic Ilesha schist belt and the Cambrian "Pan-African" Granitoids (Figure 4).

The Archean complex includes a variety of rock types, including migmatites, orthogneisses, and paragneisses, all of which have undergone metamorphism due to several orogenic events (Oyawoye 1964). According to Rahaman and Ocan (1978), the migmatite-gneiss complex falls within the medium to higher amphibolite facies.

The Ilesha schist belt is recognised for its rich mineralisation, including gold and other valuable gemstones. This schist belt is part of the Proterozoic succession within the broader Pan-African mobile belt, as described by Klemm et al.

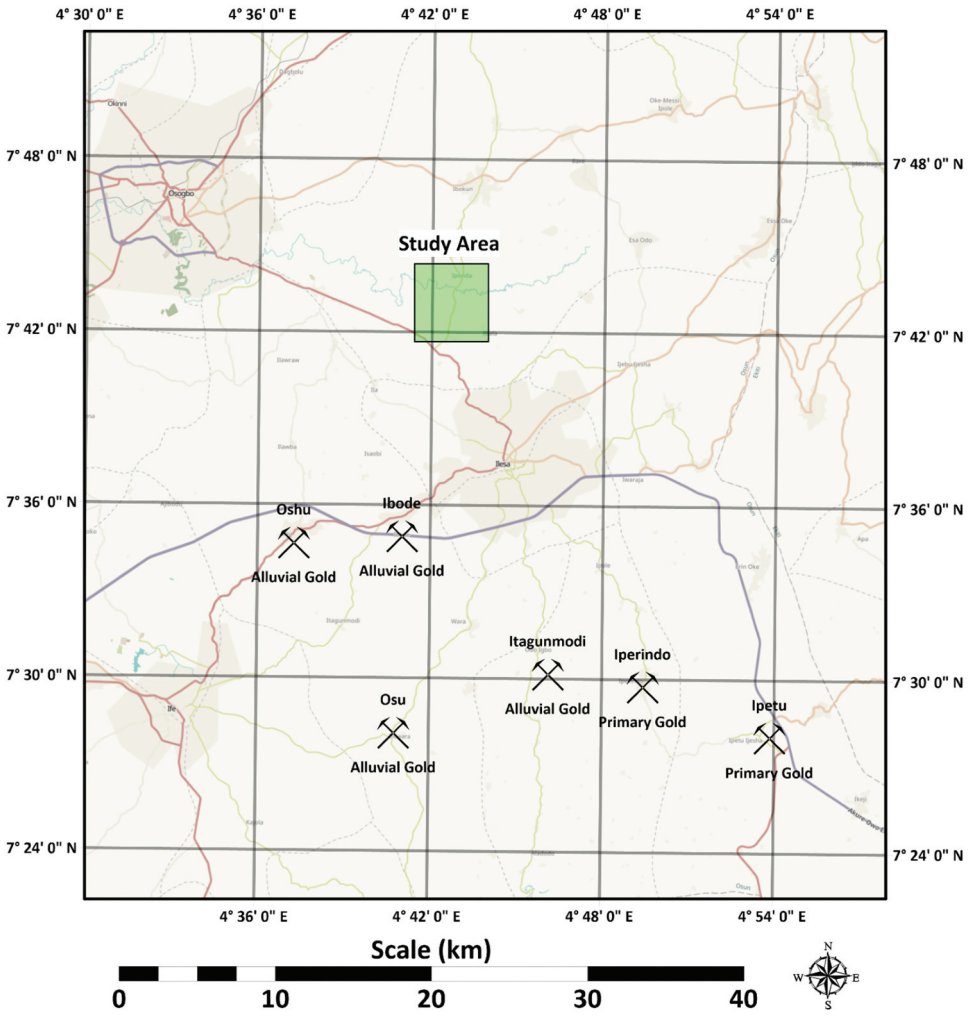

Figure 3. Map of Ilesha showing gold deposits discovered by the Nigerian Mining Corporation (NMC).

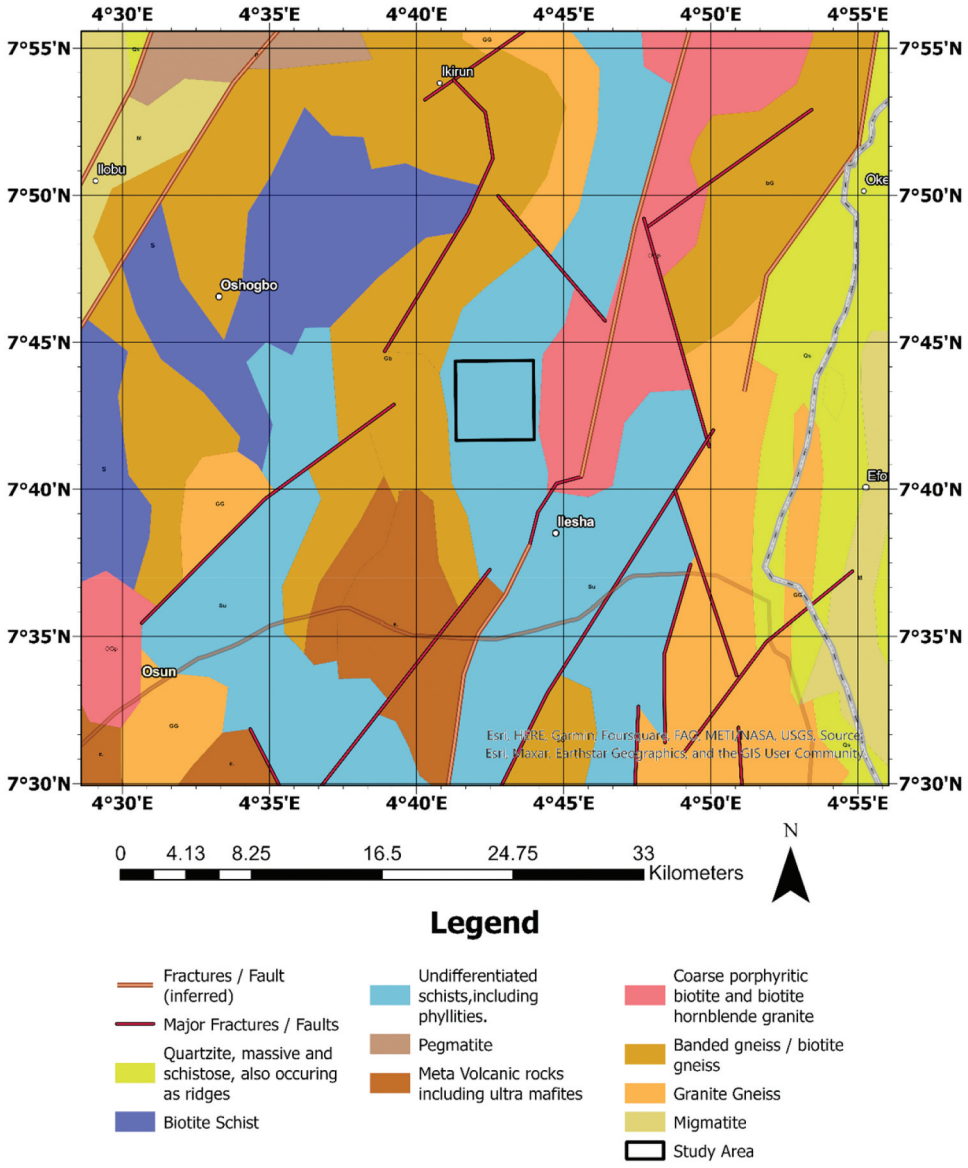

Figure 4. Regional geological map.

(1983). Elueze (1981) divided the Ilesha schist belt into the metavolcanic complex, the metapelite sequence, and the Psammitic sequence. The metavolcanic complex consists of amphibolite and ultramafic rocks, which appear as lens-shaped intrusions beneath the metapelite and psammitic sequences. These sequences represent supracrustal rocks that have experienced low to medium-grade metamorphism at temperatures ranging from 470 to 600 degrees Celsius and pressures between 3.5 and 6.0 kbar (Ige and Holness 2002). The metapelite sequence includes quartz-mica schist, biotite-garnet schist, amphibolite schist while the Psammitic sequence includes quartzite and quartz schist rich in muscovite and sericite (Elueze 1981).

The Pan-African Granitoids are granitic rocks that intrude into both the migmatite-gneiss complex and the schist belt. These granitoids include various rock types, such as pegmatites, biotite granites, charnockites, syenites, and vein quartz (Oyawoye 1964). They represent rocks formed during and after the Pan-African tectonic events.

1.3. Geology of the study area

Figure 5 shows the identified outcrops within the study area. The amphibolite schist is characterised by its darkish green colour and fine-grained texture. These outcrops are situated at low-lying positions and are exposed in streams and drainage channels. The presence of reddish overburden is attributed to haematite, which is released during the weathering of the amphibolite. Biotite schist is observed as poorly elevated outcrops, exhibiting a clear schistosity, foliation (both continuous and non-continuous types), and an abundance of biotite.

Talc-tremolite schist outcrops display a mottled creamy white colour with a pearly lustre and a slick and soapy texture. The outcrops exhibit significant weathering and numerous joints. Granite-gneiss, which is rich in biotite and muscovite, appears as

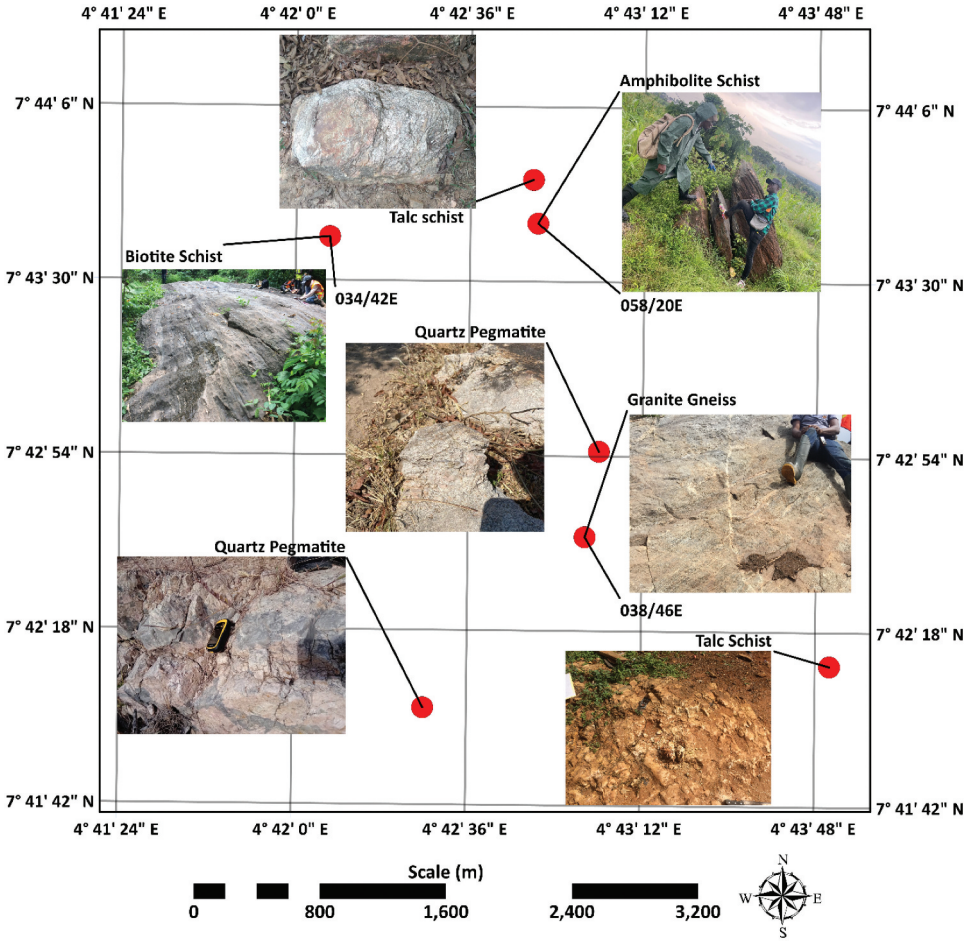

Figure 5. Map of study area showing outcrop locations.

medium-coarse grained and dark coloured. These outcrops are heavily fractured and more deformed compared to the biotite and amphibole schists. Some exposures show fractured quartz veins. The quartz pegmatite outcrops are elevated and extensive, with dominant light-coloured minerals such as plagioclase, muscovite, and quartz, alongside the presence of dark minerals like biotite. These pegmatites are genetically related to the granite-gneiss.

The major structures observed in the rocks comprise fractures, veins, and foliations. The structural orientation of the fractures and quartz veins occur in two principal directions: northeast and southeast (Figure 6). The foliation of the biotite schist is in the NE direction.

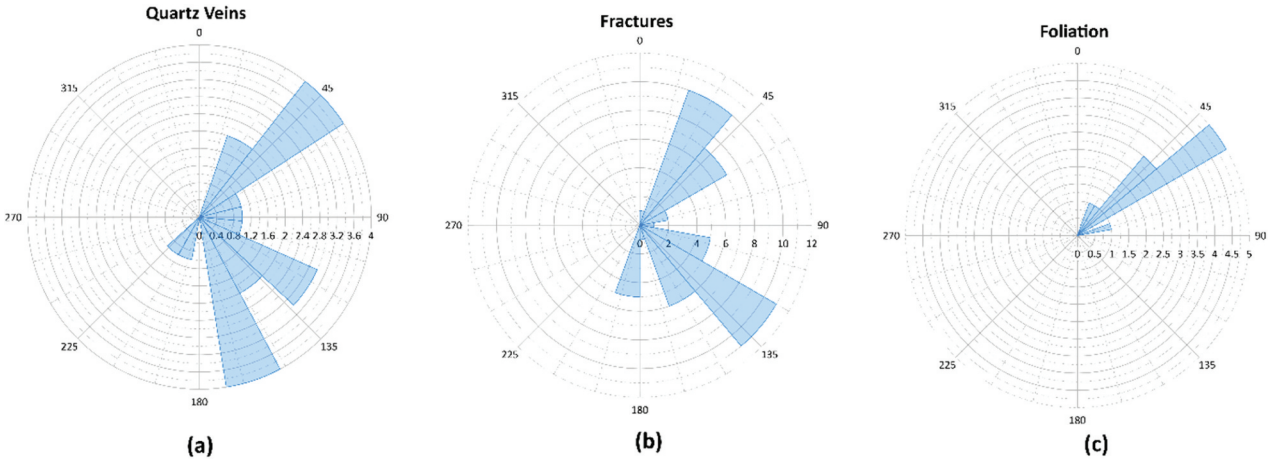

Figure 6. Rose diagram of (a) quartz veins (b) fractures (c) foliation.

2. Materials and methods

The airborne geophysical datasets, including magnetic, radiometric, and time-domain electromagnetic (TDEM) data, were obtained from the Nigerian Geological Survey Agency (NGSA). The TDEM data was collected using the TEMPEST208 digital time-domain fixed-wing EM system, flown at a 90-metre terrain clearance in a NW-SE direction, with sampling every 3 metres along flight lines spaced 200 metres apart. The Total Magnetic Field Intensity (TMI) data was acquired using up to three Scintrex Cesium vapour magnetometers mounted on a Cessna Caravan fixed-wing aircraft. The data was recorded at 7 metres intervals along NW-SE flight lines spaced 500 metres apart. Since most of the data was collected between 2005 and 2009, the IGRF 2005 model was used to calculate declination and inclination. Additionally, high-resolution airborne radiometric data was acquired using 512-channel gamma-ray spectrometers (with a NaI "Tl" crystal size of $2'' \times 2''$) mounted on a Cessna Caravan fixed-wing aircraft.

The study's approach involves three phases. In the initial phase, a thorough assessment of regional structural patterns and rock distribution is conducted. This helps enhance our understanding of the region's tectonic history. The next phase involves creating a 3D conceptual model that accurately outlines mineral system components and pinpoints exploration targets. After identifying these exploration targets using the conceptual model, the last phase comprises on-site verification and validation of the identified targets.

2.1. Phase 1: regional structural analysis

To aid in structural interpretation on a regional scale, the tilt derivative and the analytical signal mathematical filters were applied to the Total Magnetic Field Intensity (TMI) data to emphasise structural features related to the tectonic evolution of the area.

2.1.1. Tilt derivative

The tilt derivative is the angle between the first vertical and horizontal derivative (Equation 1). It is a filter with automatic gain control (AGC) that equalises the amplitude of anomalies (Stewart and Miller 2018). The tilt derivative can be used to map shallow basement structures.

$$\theta = tan^{-1} \frac{\frac{\partial T}{\partial z}}{\sqrt{\left(\frac{\partial T}{\partial x}\right)^2 + \left(\frac{\partial T}{\partial y}\right)^2}}$$

Equation 1: Tilt Derivative
Where:

$$\frac{\partial T}{\partial z} = Verticalderivativeofthemagneticfield$$

$$\frac{\partial T}{\partial x} = HorizontalderivativeinXdirectionofthemagneticfield$$

$$\frac{\partial T}{\partial y} = HorizontalderivativeinYdirectionofthemagneticfield$$

2.1.2. Analytical Signal

Nabighian (1972) proposed the concept of a 2-D analytical signal, or energy envelope, for magnetic anomalies. The analytic signal is the square root of the sum of the squares of the total magnetic field's three orthogonal gradients (Equation 2). The analytic signal is useful for locating magnetic bodies, especially when remanence and/or low magnetic latitude make interpretation difficult.

$$\boldsymbol{A} = \sqrt{\left(\frac{\partial \boldsymbol{T}}{\partial \boldsymbol{z}}\right)^2 + \left(\frac{\partial \boldsymbol{T}}{\partial \boldsymbol{x}}\right)^2 + \left(\frac{\partial \boldsymbol{T}}{\partial \boldsymbol{y}}\right)^2}$$

Equation 2: Analytical Signal
Where:

$$\frac{\partial T}{\partial z} = Verticalderivativeofthetotalmagneticfield$$

$$\frac{\partial T}{\partial x} = HorizontalderivativeinXdirectionofthemagneticfield$$

$$\frac{\partial T}{\partial y} = HorizontalderivativeinYdirectionofthemagneticfield$$

2.2. Phase 2: 3D conceptual modelling

The creation of the conceptual model involves a three-step procedure. To begin, an unsupervised classification method is implemented on the gamma-ray spectrometry data, resulting in the generation of a detailed geological map. This geological map, combined with surface outcrop data, forms the basis for constructing a 3D geological model. Following this, the attention turns towards mapping basement structures, including shear and fracture zones, in three dimensions. This objective is achieved through the application of the highly efficient 3D Euler deconvolution technique. Subsequently, the 3D magnetic inversion approach is employed to model intrusive metavolcanic bodies that might be hidden from surface observations. The outcomes of these three distinct stages are synthesised, leading to an extensive conceptual model that displays a wide variety of rock types, intricate structures, and concealed subsurface intrusions.

2.2.1. Geological mapping using Airborne gamma-ray spectrometry

An unsupervised classification of the gamma-ray spectrometry data was carried out following the

methodology outlined by Martelet et al. (2006) to create a detailed geological map. This was done using the ISO clustering procedure integrated within ArcGIS Pro. The ISO clustering technique utilises the K-mean method to extract distinct and statistically significant classes based on the concentrations of uranium (U), potassium (K), and thorium (Th) detected by the gamma-ray measurements. By correlating these classes to known outcrop, the approach becomes more capable of characterising various rock types present in the study area.

2.2.2. 3D Geological modelling

The 3D geological model utilised an implicit modelling technique, which was jointly developed by BRGM and Intrepid Geophysics. This modelling technique is grounded in the principles of potential-field theory as described by Calcagno et al. (2008). The process of implicit geological modelling involves the mapping of distinct rock units in order to define their boundaries. These boundaries are then extrapolated into the subsurface using dip information as a guiding parameter. The implicit modelling methodology employs advanced algorithms and mathematical functions to interpolate and extrapolate geological data between known data points. This computational approach enables the creation of a coherent three-dimensional representation of subsurface geology, even in regions where direct observation is limited or absent.

2.2.3. Mapping of structures using Euler 3D deconvolution method

The Euler 3D deconvolution technique is based on Euler's homogeneity equation (Equation 3), which relates the magnetic field gradients and structural index (SI) to the position of the source (Thompson 1982; Reid et al. 1990). The structural index (SI) corresponds to different geological models (for example, SI = 0 for a contact, SI = 1 for dikes and sills, and SI = 3 for spherical geobodies).

$$\frac{\partial T}{\partial x}(x - x_o) + \frac{\partial T}{\partial y}(y - y_o) + \frac{\partial T}{\partial z}(z - z_o) = SI(B - T)$$

Equation 3: Euler homogeneity equation

Where:

$$x, y, z = location\ of\ grid\ point$$

$$x_o, y_o, z_o, = location\ of\ source\ anomaly$$

$$SI = \text{Structural Index}$$

$$B = Regional\ Field$$

$$T = Total\ Magneticfield$$

2.2.4. Modelling of intrusions using 3D magnetic inversion

The 3D magnetic inversion was conducted using DSIM3D, a software implementation of an inversion method devised by Pilkington (2009). This approach aimed to determine a 3D distribution of susceptibility by analysing input magnetic anomaly data. DSIM3D accepts gridded magnetic data as input and generates a subsurface 3D model representing the magnetic susceptibilities of a uniformly spaced array of dipoles. To solve the 3D magnetic inverse problem and obtain sparse models (those with minimal nonzero values fitting the data), the inversion incorporated the Cauchy norm. This norm was employed to promote sparsity in the resulting model, ensuring simplicity and eliminating unnecessary structure except as required by the data. By minimising the number of nonzero model values, the approach penalised smooth variations and encouraged a more compact character in the solution. For further details regarding the algorithm, refer to the work by Pilkington (2009).

2.2.5. Identifying exploration targets using conductivity depth imaging (CDI)

The airborne time domain electromagnetic TDEM data provide valuable early insights for identifying auriferous basement structures, which often exhibit conspicuous high-conductivity anomalies easily distinguishable on the CDI sections (Osinowo et al. 2021).

2.3. Phase 3: ground truthing

The Geoelectric survey was used to validate the exploration targets identified in phase 2. The resistivity and induced polarisation (IP) measurements were acquired using the dipole-dipole array configuration with an electrode spacing of 5 metres at a spread of 200 to 300 metres. The IP and resistivity data was processed using the Res2dinv software.

3. Results

3.1. Regional structural interpretation

The regional structural pattern was analysed using the tilt ratio (Figure 7) and analytical signal (Figure 8) filters applied to the total magnetic intensity (TMI) data. This analysis revealed two prominent structural trends: northeastern structures (D1) and north-northeast structures (D2), as shown in Figure 9. Caby and Boesse (2001) associated both trends with the Pan-African orogeny, which caused significant deformation in a northeastern direction, visible as magnetic lineation on the tilt ratio map. The D1 structures are late-stage mafic dykes that intrude various rock types, while the D2 structures are shear zones containing high-temperature mylonite, quartz veins, and pegmatites (Caby and Boesse 2001).

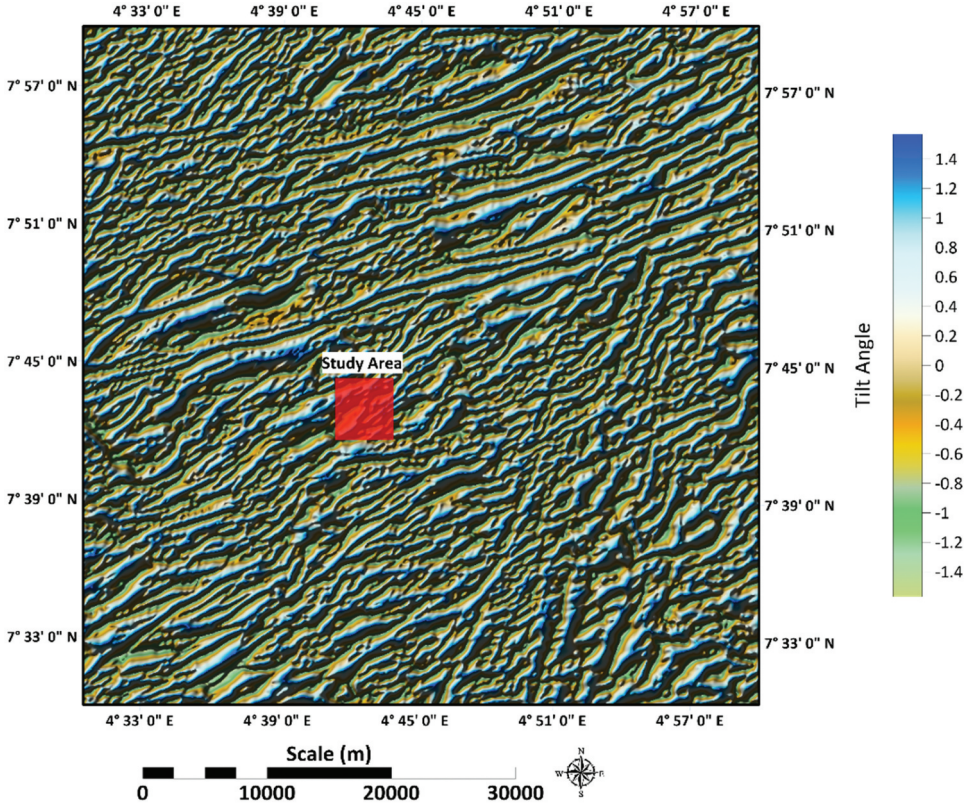

Figure 7. Tilt ratio map.

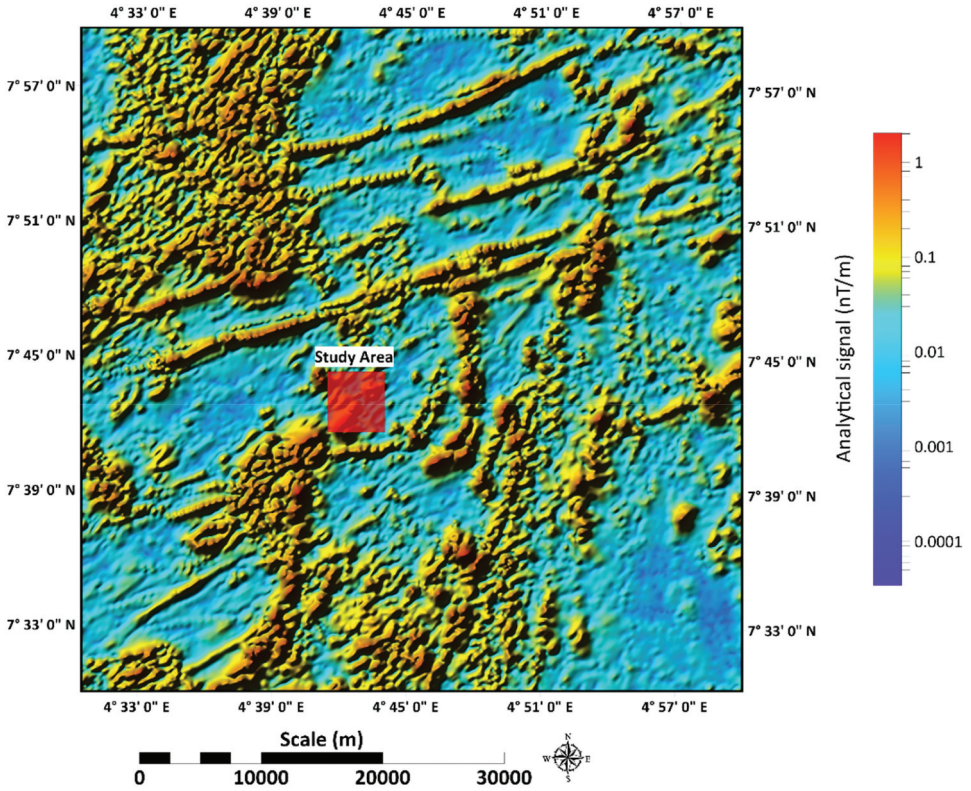

Figure 8. Analytical signal map.

3.2. Regional metavolcanic complex

The analytical signal map effectively highlights the presence of metavolcanic rocks, evident as high-amplitude anomalies, as depicted in Figure 10. This heightened magnetic amplitude is a direct consequence of the metavolcanic rocks' substantial content of Fe-Ti oxides. The unique geological history of these rocks, characterised by slow cooling, has allowed for

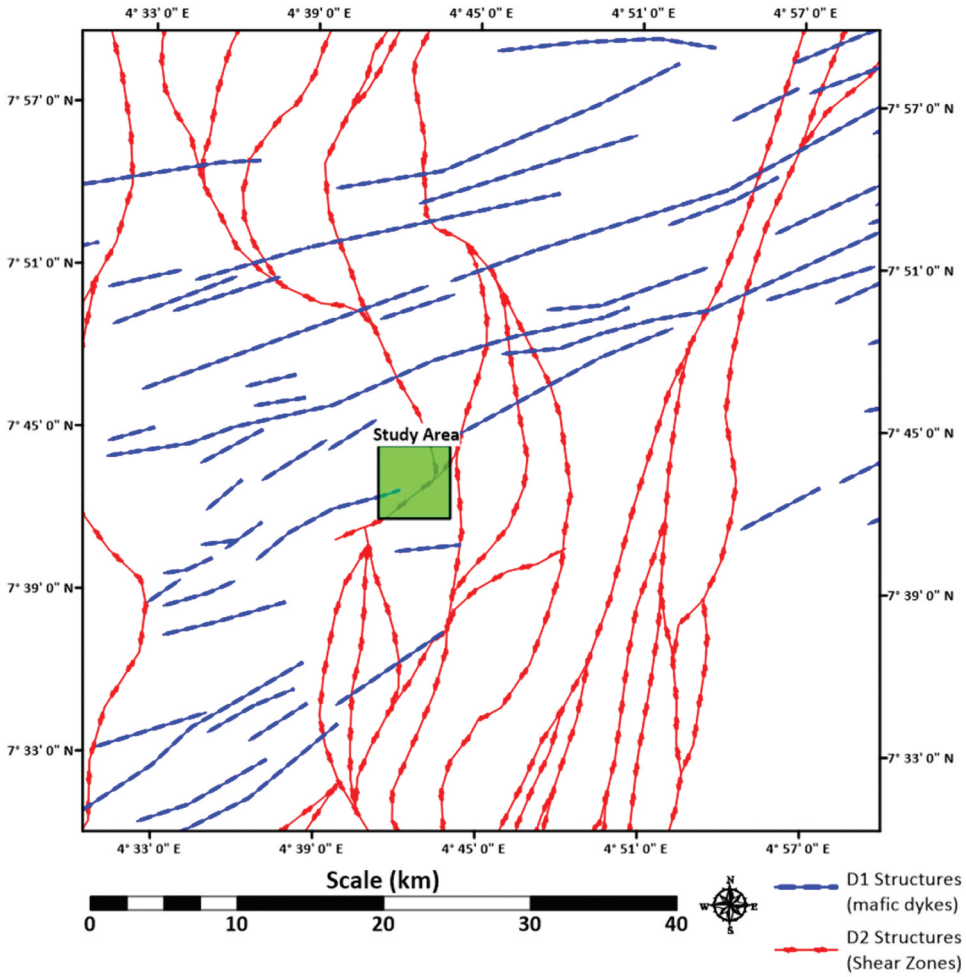

Figure 9. Structural map depicting D1 and D2 structures.

the enrichment of Fe-Ti oxides through the replacement of previously crystallised pyroxenes by late-igneous amphiboles (Ige et al. 1998). On outcrops, the metavolcanic rocks include massive, banded schistose and strongly gneissic textural types. Ultra-mafic rocks have been reported to occur as boudins spatially associated with the metavolcanic rocks (Klemm et al. 1983). The metamorphic grade is in the lower amphibolite facies (Olade and Elueze 1979).

Ige et al. (1998) concluded that the metavolcanic complex was derived from a series of thick, highly differentiated, basaltic sills. The slow cooling of the basaltic sills enabled crystal settling giving rise to the formation of ultramafic cumulates at the base of the basaltic sills. The subsequent enrichment of volatiles at the apex of the basaltic sills facilitated the formation of Fe-Ti oxides, sulphides, and apatite, as well as late-magmatic amphibole.

In the mineral systems context, metavolcanic rocks have emerged as significant sources of valuable metals, particularly in orogenic gold deposits, as suggested by previous research works such as Henley et al. (1976); Bierlein and Pisarevsky (2008); and Bierlein and Craw (2008). Analysing metavolcanic rocks from southwest Nigeria using Atomic Absorption Spectroscopy (AAS) has revealed noteworthy concentrations of gold, a discovery documented by Bafor (1981) and Garba (1988). These observations have contributed to the consideration of metavolcanic rocks as potential metal sources within the Ilesha goldfields, a notion explored by Oyinloye (2006) and Garba (1988).

3.3. Conceptual Model

3.3.1. Geology Map

The Unsupervised classification of the radiometric ternary map resulted in five categories (Figure 11). Each category's statistical summary is presented in Table 1. Based on the outcrop location, each class was found to correspond to a distinct type of rock (Figure 12). Class 1 represents a mafic schist rock type, encompassing both amphibolite schist and biotite schist outcrops. Its average concentrations of K, Th, and U were determined to be 0.30%, 8.93 ppm, and 1.90 ppm, respectively. Class 2, interpreted as a talc-tremolite rock type, comprises talc-tremolite schist outcrops, with average K, Th, and U concentrations of 0.27%, 6.42 ppm, and 1.21 ppm, respectively. The lower levels of K, Th, and U in talc-tremolite schist compared to mafic schist were

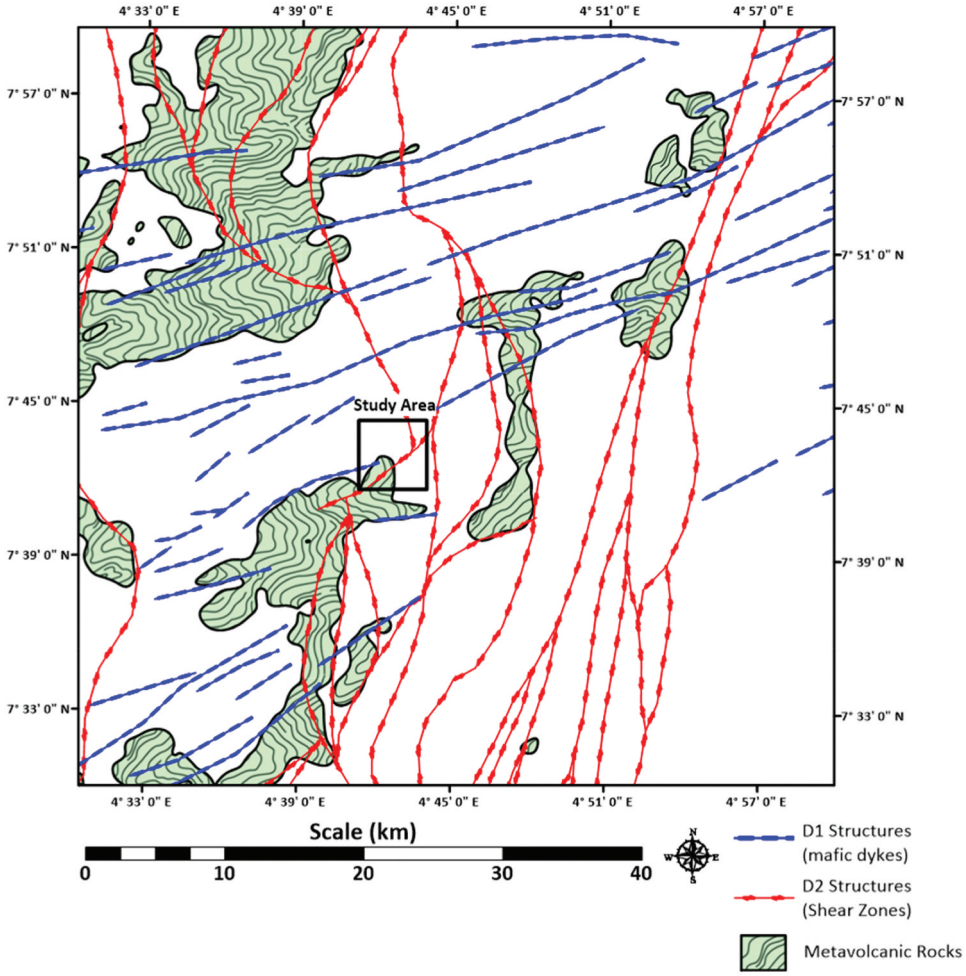

Figure 10. Map of metavolcanic rocks derived from the analytical signal map.

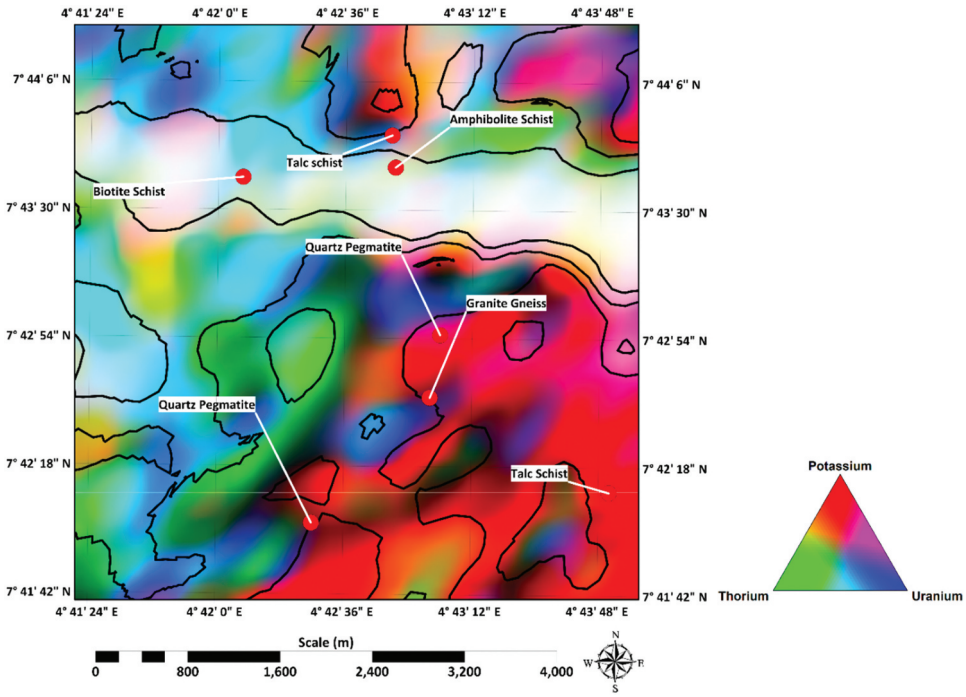

Figure 11. Radiometric ternary map showing class boundaries and outcrop locations.

Table 1. Statistical summary of each class.

Class	Interpreted Rock Type		Min Value	First Quartile	Median Value	Third Quartile	Max Value	IQR
1	Mafic schists	K	0.13	0.22	0.30	0.39	1.05	0.17
		Th	4.93	7.90	8.93	10.79	17.00	2.89
		U	0.69	1.62	1.90	2.22	3.47	0.59
2	Talc-tremolite schist	K	0.14	0.22	0.27	0.34	0.92	0.12
		Th	3.04	5.37	6.43	7.49	12.43	2.13
		U	−0.21	0.84	1.21	1.53	2.69	0.69
3	Granite Gneiss	K	0.18	0.27	0.32	0.37	0.67	0.10
		Th	0.87	3.58	4.29	5.18	8.36	1.60
		U	−0.21	0.52	0.77	1.01	1.87	0.49
4	Alluvium	K	0.18	0.45	0.62	0.81	1.33	0.36
		Th	7.28	12.45	14.37	16.59	21.02	4.14
		U	1.60	2.63	3.08	3.56	4.64	0.94
5	Felsic schist	K	0.18	0.45	0.62	0.81	1.33	0.36
		Th	7.28	12.45	14.37	16.59	21.02	4.14
		U	1.60	2.63	3.08	3.56	4.64	0.94

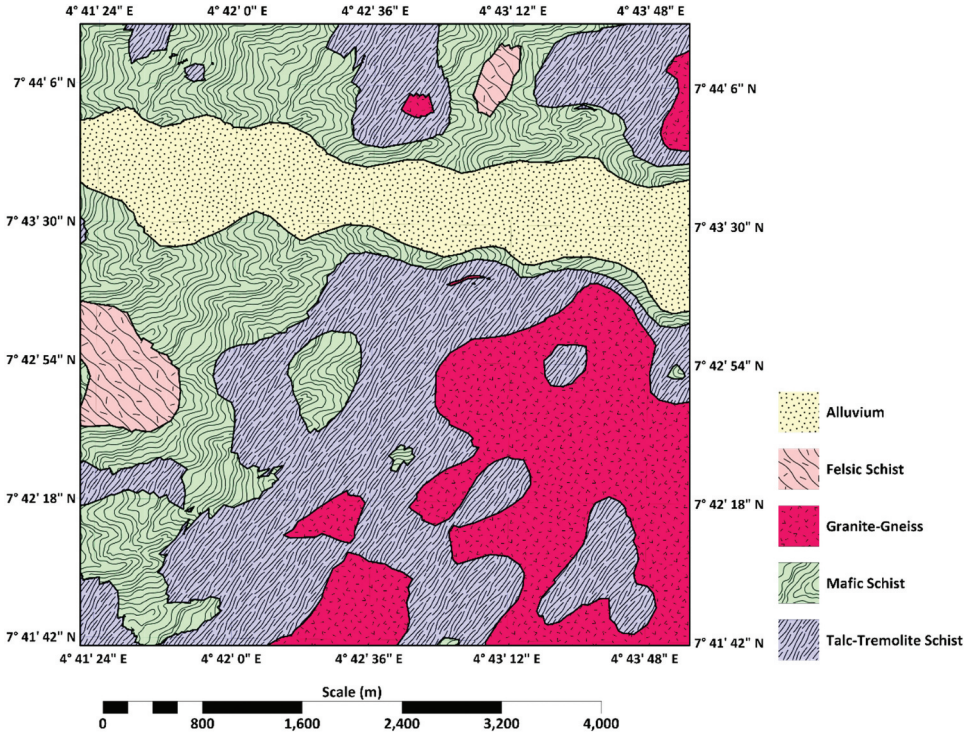

Figure 12. Geological map derived from unsupervised classification of the ternary map.

attributed to the abundance of talc and tremolite minerals compared to the more radioactive biotite and amphibole minerals.

Class 3 represents a granite-gneiss rock type, including granite-gneiss and quartz pegmatite outcrops, with average K, Th, and U concentrations of 0.32%, 4.29 ppm, and 0.76 ppm, respectively. The relatively higher K concentrations were attributed to the abundance of K-feldspars. On the other hand, Class 4, associated with the Oyile River, was identified as recent fluvial deposits. Its average concentrations of K, Th, and U were determined to be 0.62%, 14.37 ppm, and 3.08 ppm, respectively. Class 5, although lacking associated outcrops, exhibited relatively high K, Th, and U concentrations, suggesting a composition of felsic minerals, therefore; class 5 was interpreted to be a felsic schist rock type.

3.3.2. Geological Model

The outcome of the implicit geological modelling is depicted in Figure 13 . The primary rock types identified are the mafic schist and talc-tremolite schist. The talc-tremolite schist overlies the mafic schist with the rock boundary dipping towards the southeast at an approximate angle of 31 degrees (Figure 14). Additionally, the talc-tremolite schist has been intruded by granite gneiss. Within the mafic schists, localised occurrences of felsic schist are observed. This represents facies changes in the protolith of the mafic schist before undergoing metamorphism. The alluvial deposits consist of weathered materials derived from the schists and granites.

3.3.3. Meta volcanic Intrusions

The detection of metavolcanic intrusions was accomplished by utilising the susceptibility volume

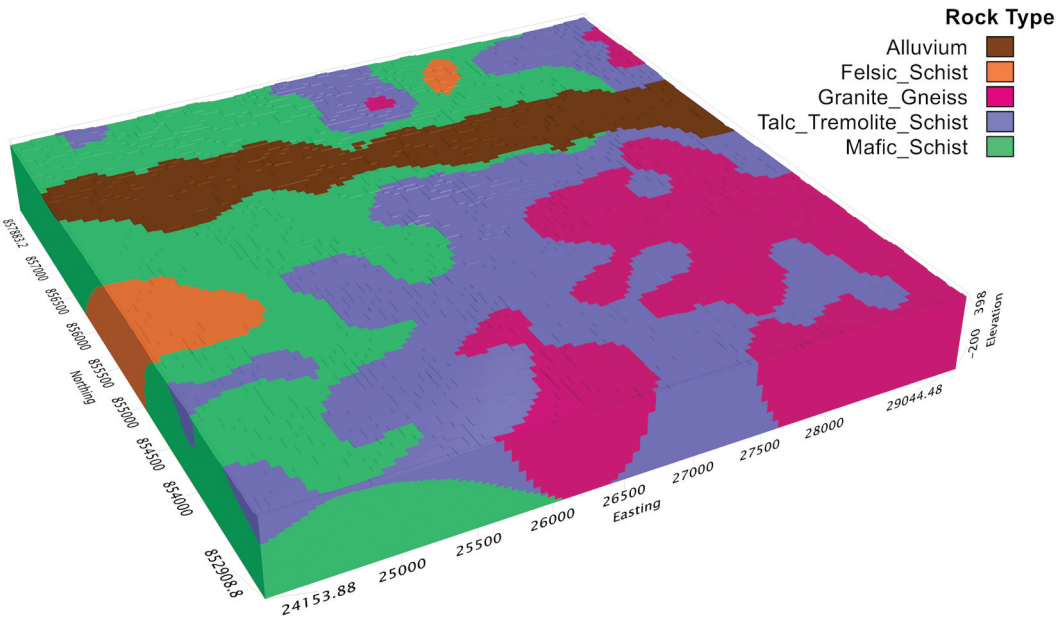

Figure 13. 3D geological model of study area

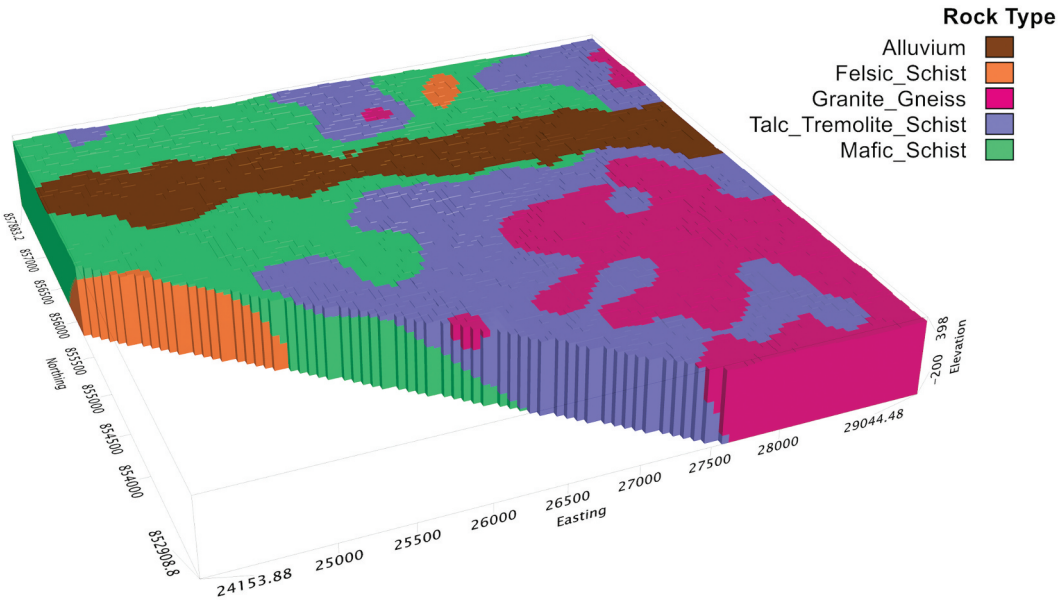

Figure 14. Clipped geological model showing rock boundaries.

derived from the three-dimensional inversion of aeromagnetic data (Figure 15). A threshold isosurface at 0.012 SI reveals a series of distinct geobodies trending towards the northeast (Figure 16). These geobodies represent metavolcanic intrusions characterised by a significant presence of magnetite. These intrusions manifest as boudins attributed to the metamorphic deformation undergone by the metavolcanic intrusions.

3.3.4. Structural model

The Euler deconvolution technique has been employed to map the basement structures, as displayed in Figure 17 . These structures exhibit two prominent orientations: the northeast and north-northeast directions. These orientations correspond to the D1 and D2 regional structural trends, which are depicted in the regional structural map (Figure 10). The northeast structure aligns with the D1 structures, interpreted to be mafic dykes, while the north-northeast structure corresponds with the D2 structures, interpreted to be shear zones (Figure 18).

These structures have been categorised into three fracture zones: the northwestern, central, and southeastern zones (Figure 19). Generally, the northwestern fracture zone is situated at the greatest depth, with an average of 300 metres, while the southeastern fracture zone is shallower, averaging around 120 metres. Within the central fracture

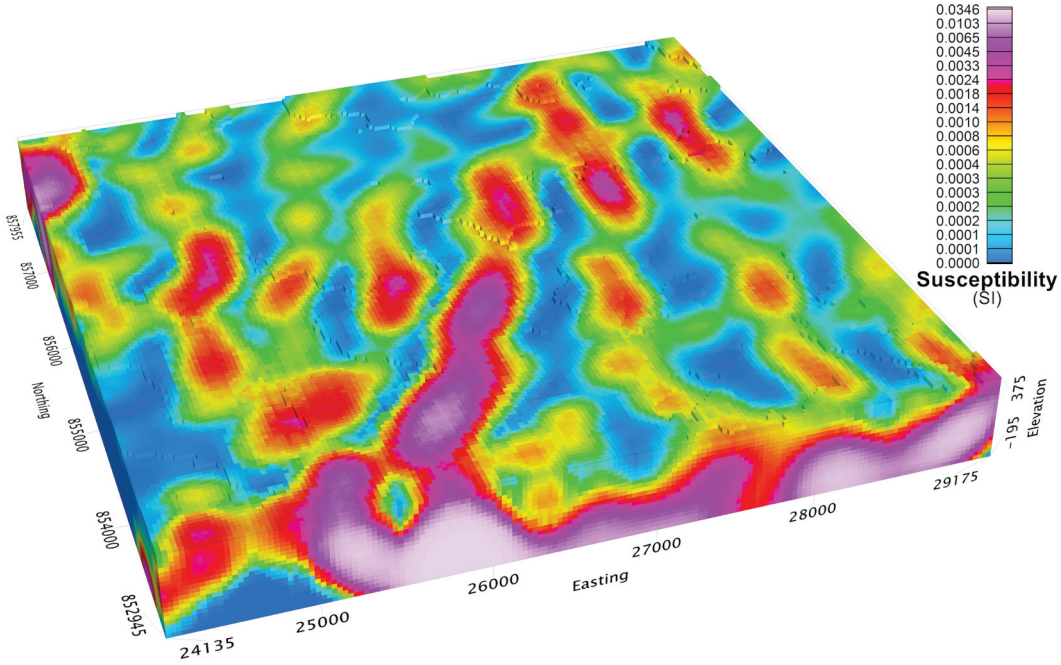

Figure 15. 3D susceptibility model of study area.

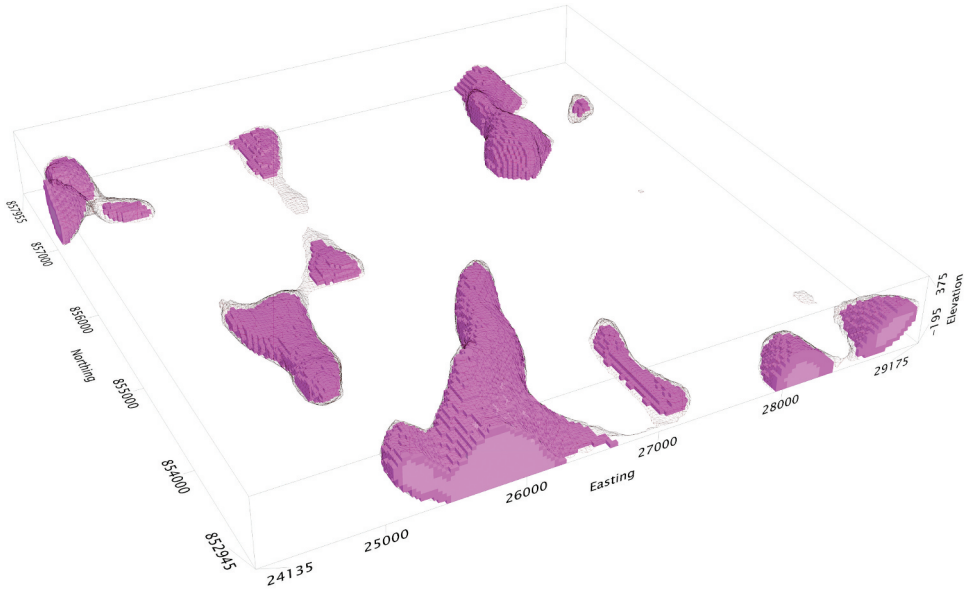

Figure 16. Clipped susceptibility model showing iso-surface at 0.012 SI.

zone, D2 structures occur at a depth of less than 100 metres, in contrast to the D1 structures that exist at an average depth of 260 metres.

When combining the structural model with the geological model, it becomes evident that these structures are not confined to any specific rock type. However, the D1 structure within the central fracture zone coincides with the boundary between the talc tremolite schist and the biotite schist (Figure 20).

3.3.5. Exploration Targets

The targeting of auriferous structures in the Iperindo and Ipetu deposits involved using pyrite, a prevalent gangue mineral, as an indicator. Utilising the notable conductive properties of pyrite, conductivity depth images (CDI) derived from time domain electromagnetic (TDEM) data were utilised for the purpose of detecting conductivity anomalies associated with pyrite -enriched fractures (Figure 21and Figure 22).

The D2 structure in the central fracture zone displays a notable conductivity anomaly, represented by a 1.6 mS/m isosurface (Figure 23 andFigure 24). Additionally, the L-shaped structure, which encompasses both D1 and D2 structures, also exhibits a significant conductivity anomaly. Some minor conductivity anomalies are not spatially connected to any specific structure.

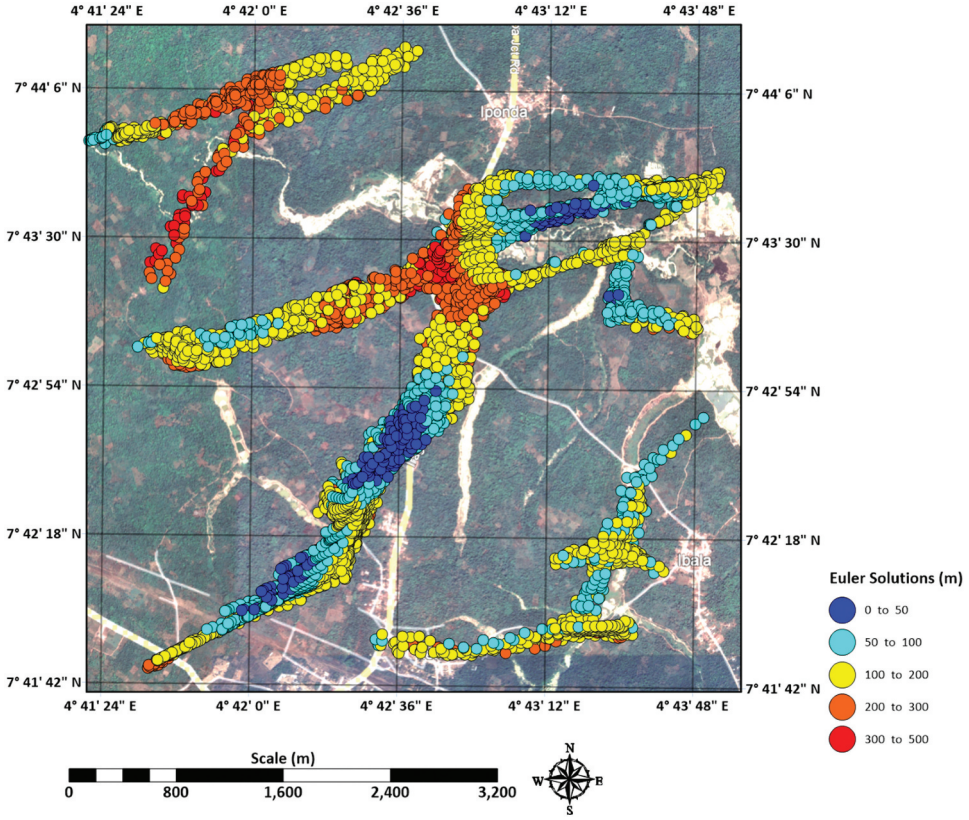

Figure 17. Map of Euler solutions.

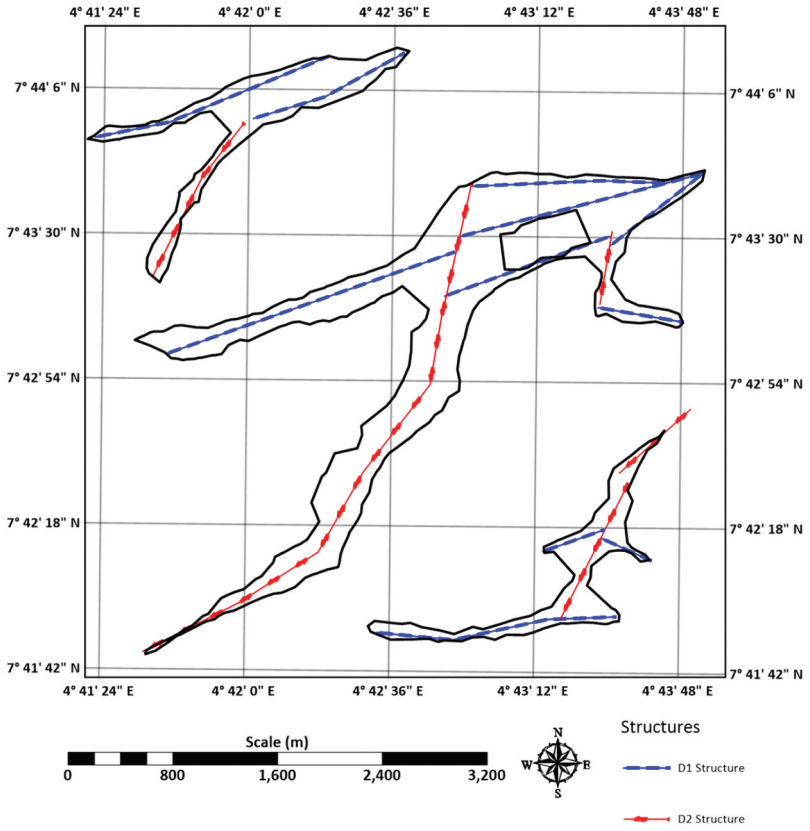

Figure 18. Structural Interpretation of Euler solutions.

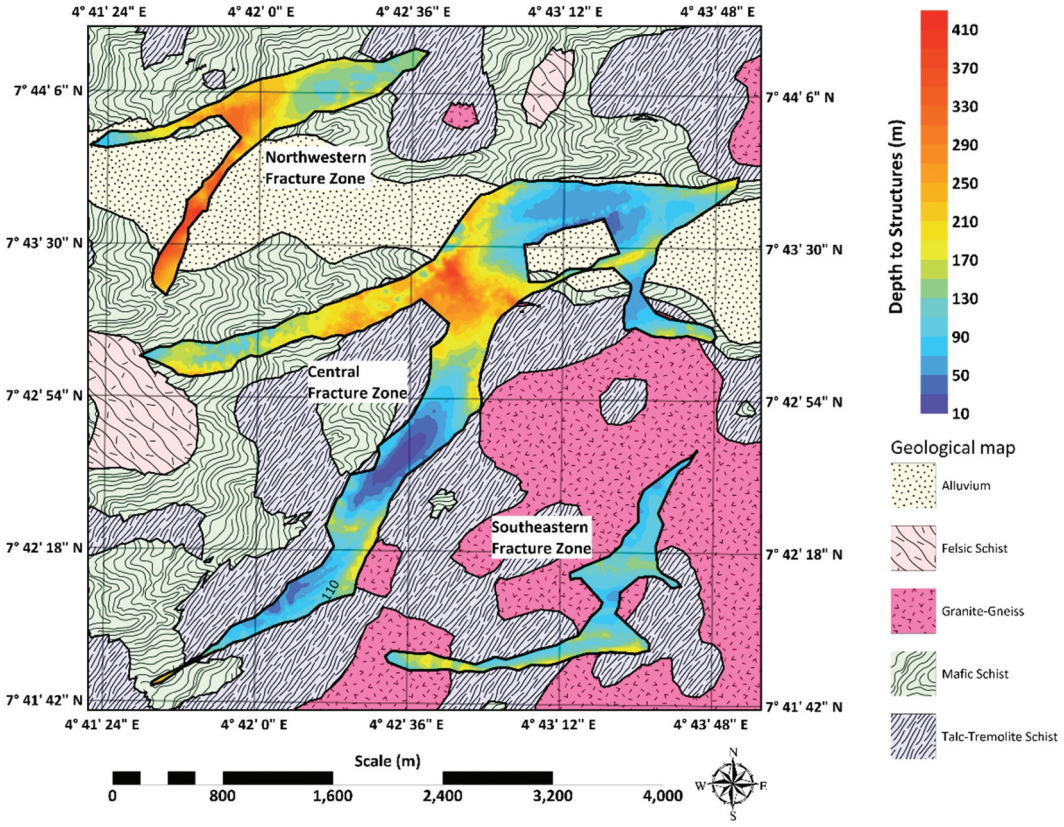

Figure 19. Depth to fracture zones overlain on geological map.

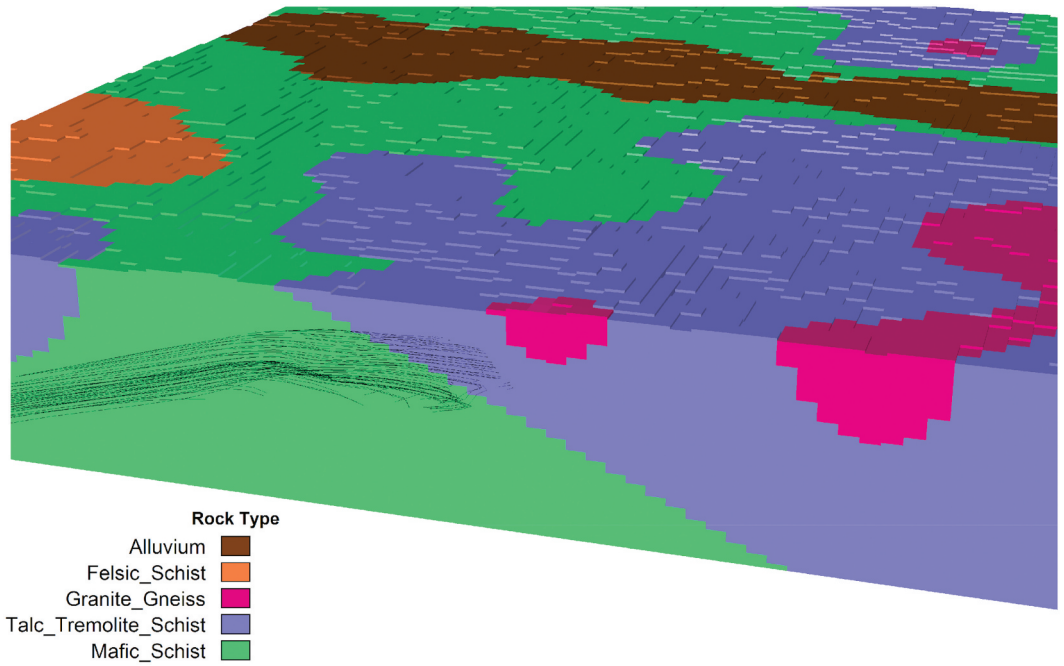

Figure 20. Clipped geological model showing structures coincident with the boundary between the talc tremolite schist and the biotite schist.

4. Discussion

4.1. Mineral System

The mineral system within the study area was characterised using the metamorphic devolatilisation model (Kerrich and Fryer 1979; Kerrich and Fyfe 1981; Phillips and Groves 1983; Goldfarb et al. 1986, 1988; Colvine et al. 1988). In this model, gold and other ore components were considered to have been released during the transition from greenschist to amphibolite facies metamorphism (Powell et al. 1991; Tomkins 2010). The metamorphic devolatilisation model can be segmented into three components: the source region, migration pathways, and deposition

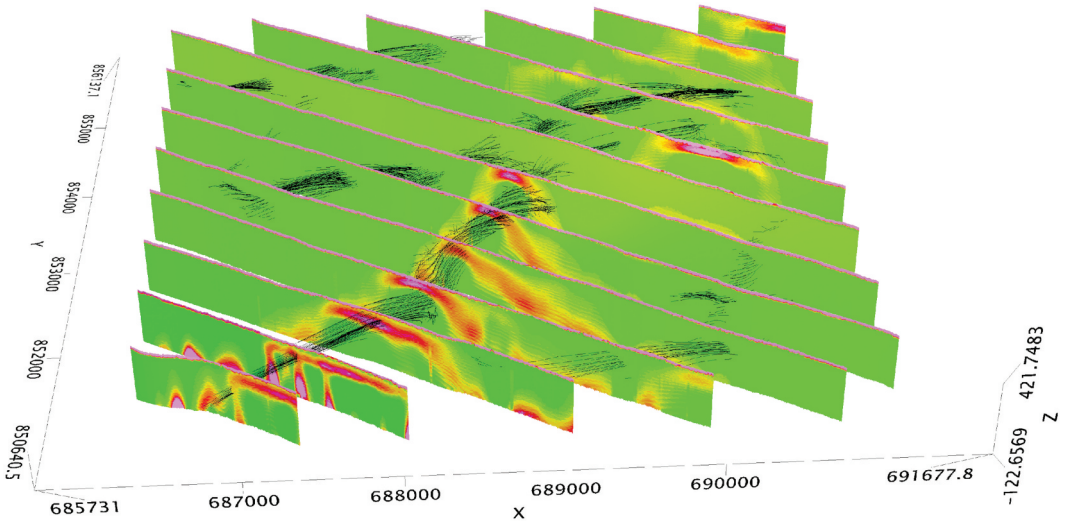

Figure 21. 3D conductivity sections (CDI) showing conductivity anomaly associated with the D2 structure in the central fracture zone.

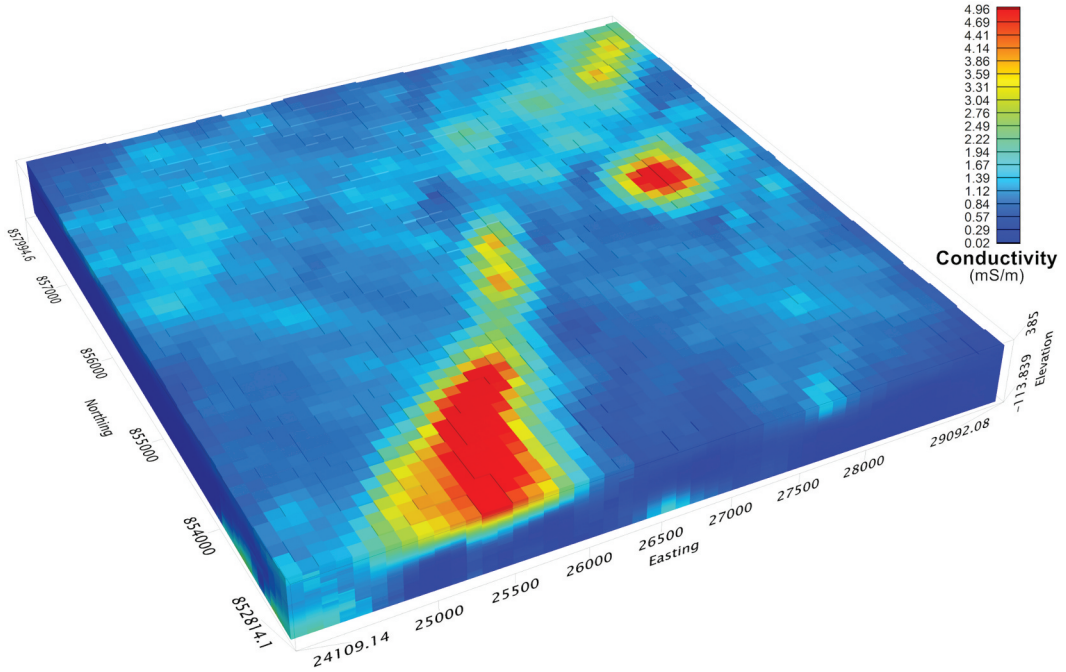

Figure 22. 3D conductivity model derived from gridded conductivity sections (CDI).

mechanism. The source regions include the origins of both the fluids and the gold. The migration pathways are fractures, faults and shear zones through which gold-enriched fluids are transported from their source regions to the sites of deposition. The deposition mechanism is physio-chemical processes that lead to the precipitation of gold from the transporting fluids during migration.

4.2. Source Region

Metavolcanic rocks have been suggested to be important source rocks for fluids and metals in orogenic gold deposits (Henley et al. 1976; Phillips et al. 1987; Garba 1988; Bierlein and Craw 2008; Bierlein and Pisarevsky 2008; Hronsky et al. 2012; Wyman et al. 2016). Elmer et al. (2006) demonstrated that metamorphism of mafic volcanic rocks has the potential to transform up to 5% of the rock's mass into metamorphic fluid, distinguished by its low salinity and a composition abundant in H2O – CO2–H2S. Phillips and Powell (2010), on the other hand, determined that this H2O – CO2–H2S-rich fluid is capable of generating sulphur complexes with the ability to extract around 3 to 15 tons of gold per cubic kilometre of mafic volcanic rock.

The metavolcanic intrusion located near the central fracture zone is identified as a potential source region (Figure 25). With the intrusion's volume measuring 0.42 cubic kilometres, an initial estimation suggests that around 1.26–6.3 tons of gold were expelled by the metavolcanic intrusion during the metamorphic devolatilisation process.

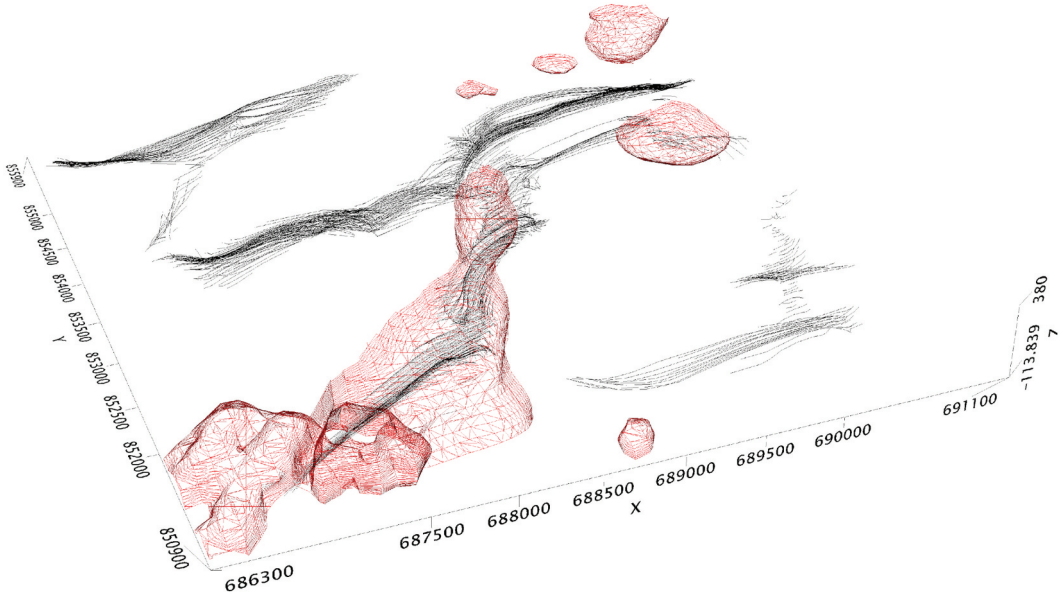

Figure 23. 3D structural model showing 1.6 mS/m isosurface.

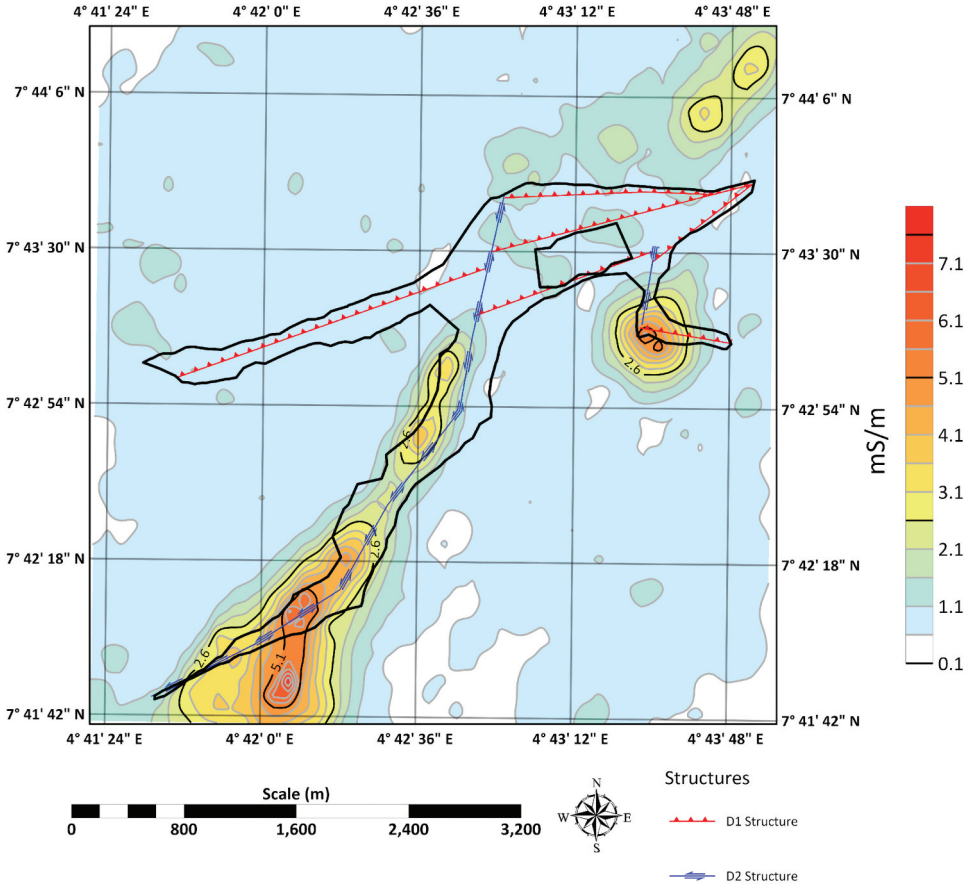

Figure 24. Map of central fracture zone showing conductivity depth slice at 100m bgl.

4.3. Fluid Migration

In the study area, the central fracture zone served as the preferred pathway for the migration of the auriferous metamorphic fluid (Figure 26). This preference can be attributed to the intersection of the central fracture zone with the metavolcanic rock. This intersection effectively functioned as the conduit through which the auriferous metamorphic fluids, released by the metavolcanic rock, were able to migrate into the central fracture system.

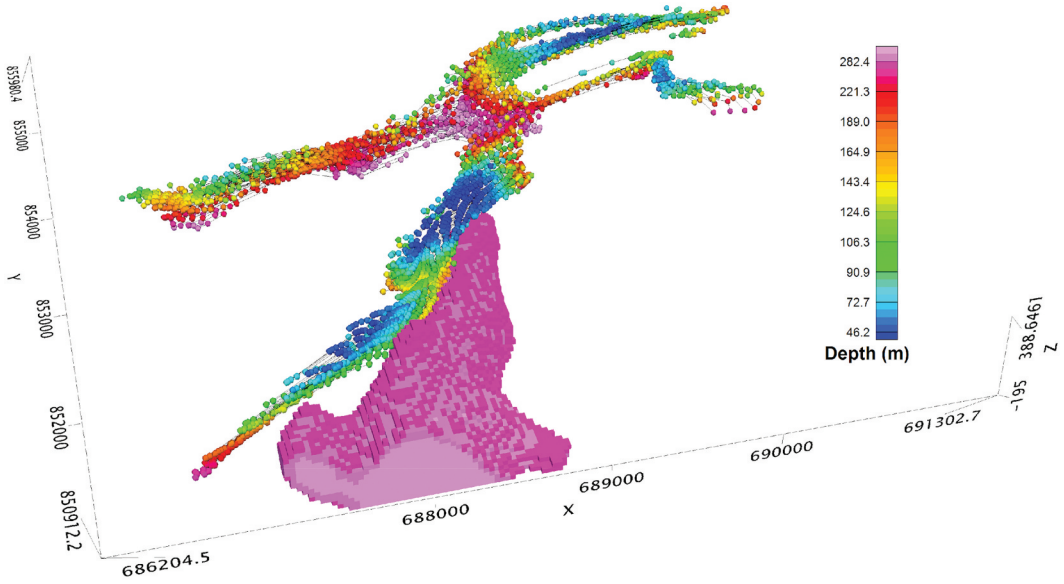

Figure 25. 3D model of central fracture zone showing metavolcanic intrusion.

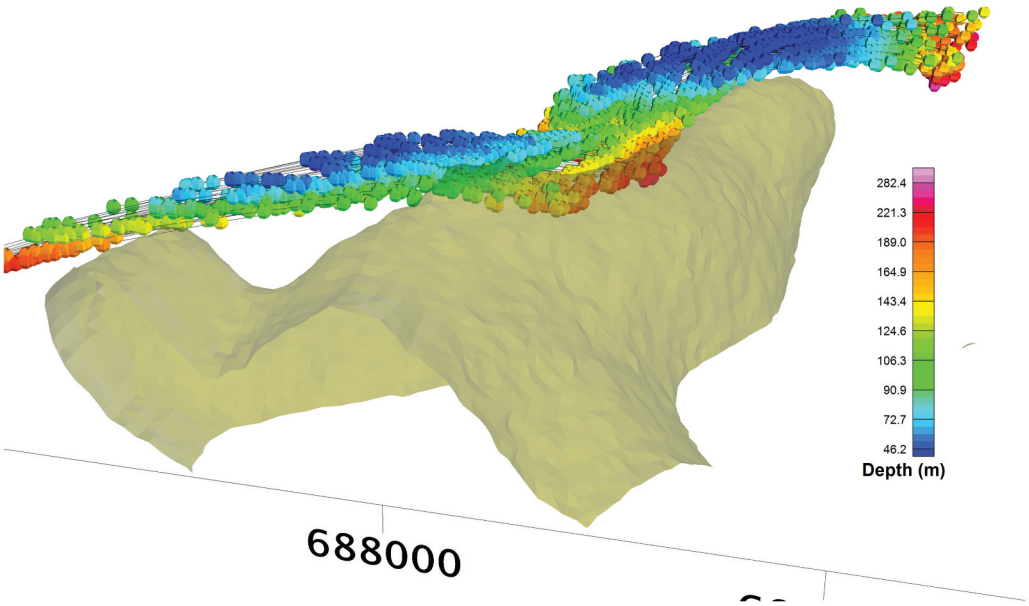

Figure 26. 3D model of central fracture zone showing intersection with metavolcanic intrusion.

4.4. Gold Deposition

The process of gold deposition is most effectively accomplished through Wall rock sulphidation (Phillips and Powell 2010). Mafic host rocks are particularly well-suited for this process, as the iron contained in these rocks can react with sulphur present in the auriferous metamorphic fluid, resulting in the formation of pyrite. This interaction consumes sulphur, which in turn diminishes the capacity of the metamorphic fluid to carry gold, consequently causing gold to precipitate out. This specific mechanism of gold deposition leads to the simultaneous formation of pyrite as an additional mineral alongside the gold. The occurrence of pyrite as a frequently found gangue mineral in both the Iperindo and Ipetu deposits serves as evidence supporting this process of gold precipitation. The high electrical conductivity observed in the central fracture zone indicates the presence of pyrite linked to gold deposition (see Figure 27).

To summarise, employing the mineral system approach, the D2 structure in the central fracture zone has been confirmed as a viable target for exploration. The major elements of a gold mineral system have been identified through geological, susceptibility, and conductivity models (Figure 28). The gold is thought to have been sourced from the metavolcanic intrusion then conveyed into the fracture zone. As the gold-bearing fluid moved along the fracture zone, the interaction between the auriferous fluid and the iron present in the mafic schist resulted in the precipitation of gold along with pyrite (Figure 29).

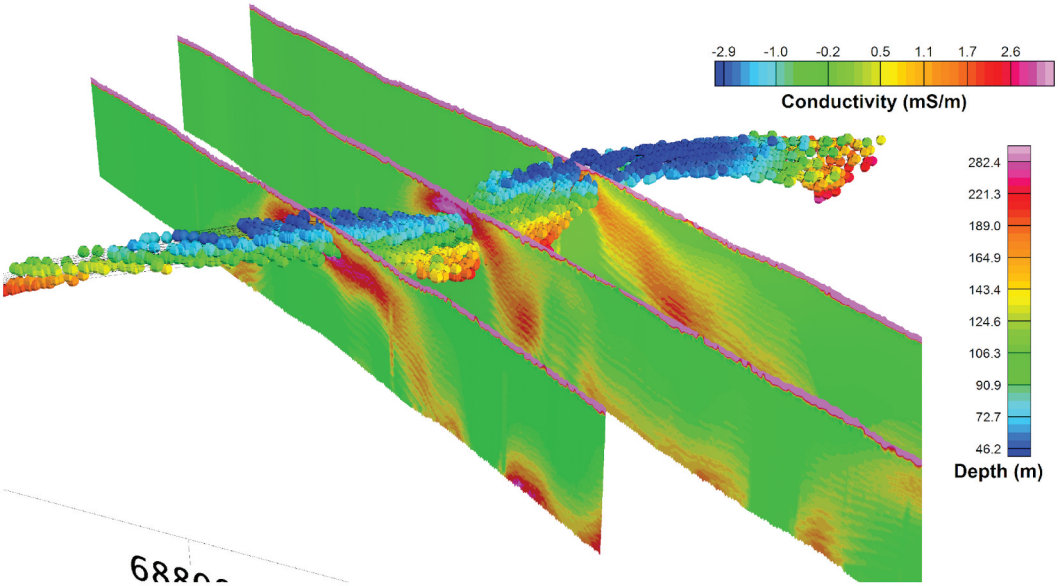

Figure 27. 3D model of central fracture zone showing anomalous conductivity indicating the presence of pyrite.

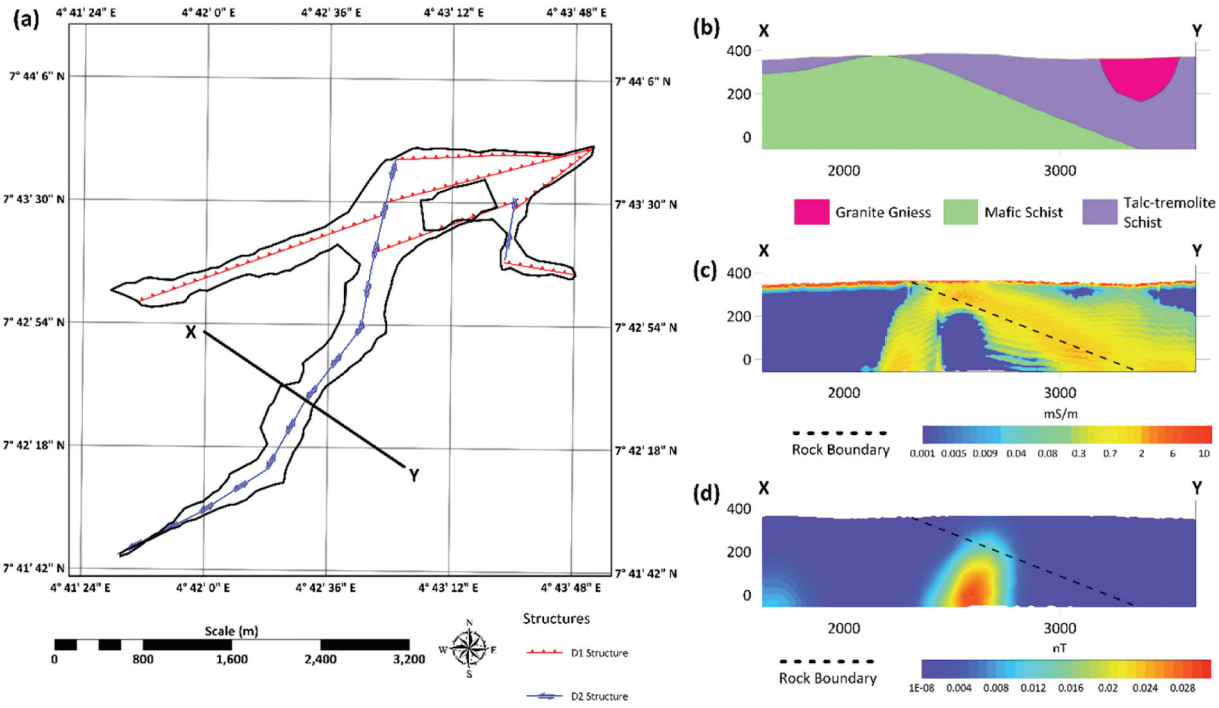

Figure 28. (a) map of central fracture zone showing cross section. (b) geological cross section. (c) conductivity cross section. (d) susceptibility cross section.

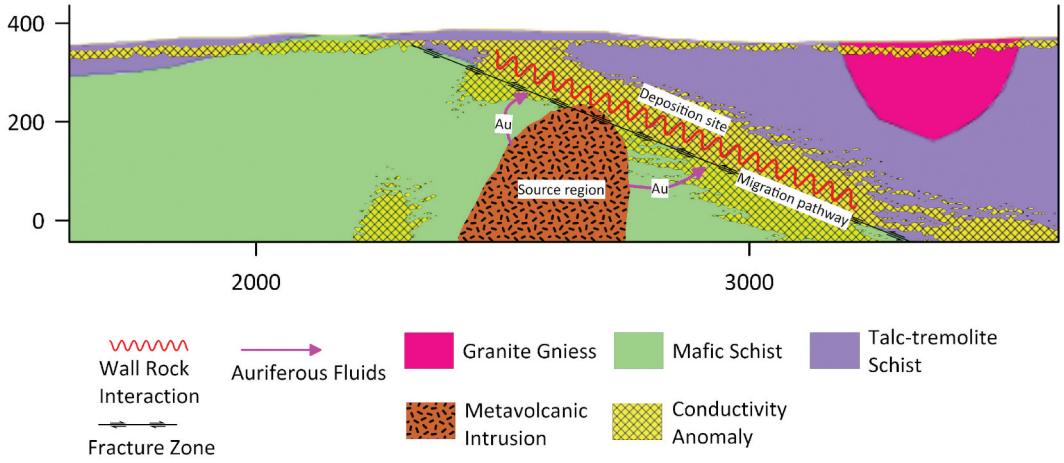

Figure 29. Cross section showing proposed mineral system of the study area.

4.5. 4.5 Source of the alluvial gold deposits

The origin of alluvial gold must meet three primary prerequisites. Firstly, it must be situated at a high topographic elevation. Secondly, the depth to the structure at the source location should be within the shallow weathering horizon. Thirdly, the conductivity of the structure should exhibit relatively high values, as this signifies the presence of pyrite, a mineral indicative of potential gold deposits. To identify the source location, a site suitability analysis was conducted. This involved integrating the depth to structure map, the topographic map, and the conductivity map (Figure 30).

The topographic map was employed to highlight elevated regions within the central fracture zone. Within the depth to structure map, areas exhibiting depths less than 50 metres were identified as potential source sites, as these structures would be situated shallow enough to undergo weathering and subsequent erosion. The conductivity map was used to identify areas with conductivity values exceeding 2 mS/m, indicating the likelihood of pyrite occurrence. Ultimately, regions where the highlighted zones on the topographic, conductivity and structural maps coincided were delineated as potential source locations for alluvial gold.

Three potential source regions were identified, and to confirm these areas as the origins of alluvial gold, a drainage assessment was conducted. This involved utilising the topographic map to outline the likely pathways taken by weathered auriferous materials during weathering and erosion. Within the suggested source regions, specific points were digitally marked to simulate the presence of weathered gold-bearing materials. Subsequently, the movement of these points was tracked as they were carried out of the study area by means of drainage channels (Figure 31).

The findings from the drainage analysis indicated that the proposed source regions indeed had the capability to provide the alluvial mines with weathered materials containing gold. Nonetheless, it became apparent that the gold within the abandoned mine did not originate from within the study area itself, but rather from auriferous structures situated further south. This could potentially explain the reason behind the abandonment of the mine, as it wasn't adequately supplied with gold by nearby auriferous structures. Furthermore, the drainage analysis also proved valuable in identifying alluvial gold deposits that had been overlooked or not properly explored (Figure 32).

5. Ground truthing

Two electrical resistivity tomography (ERT) and induced polarisation (IP) profiles were carried

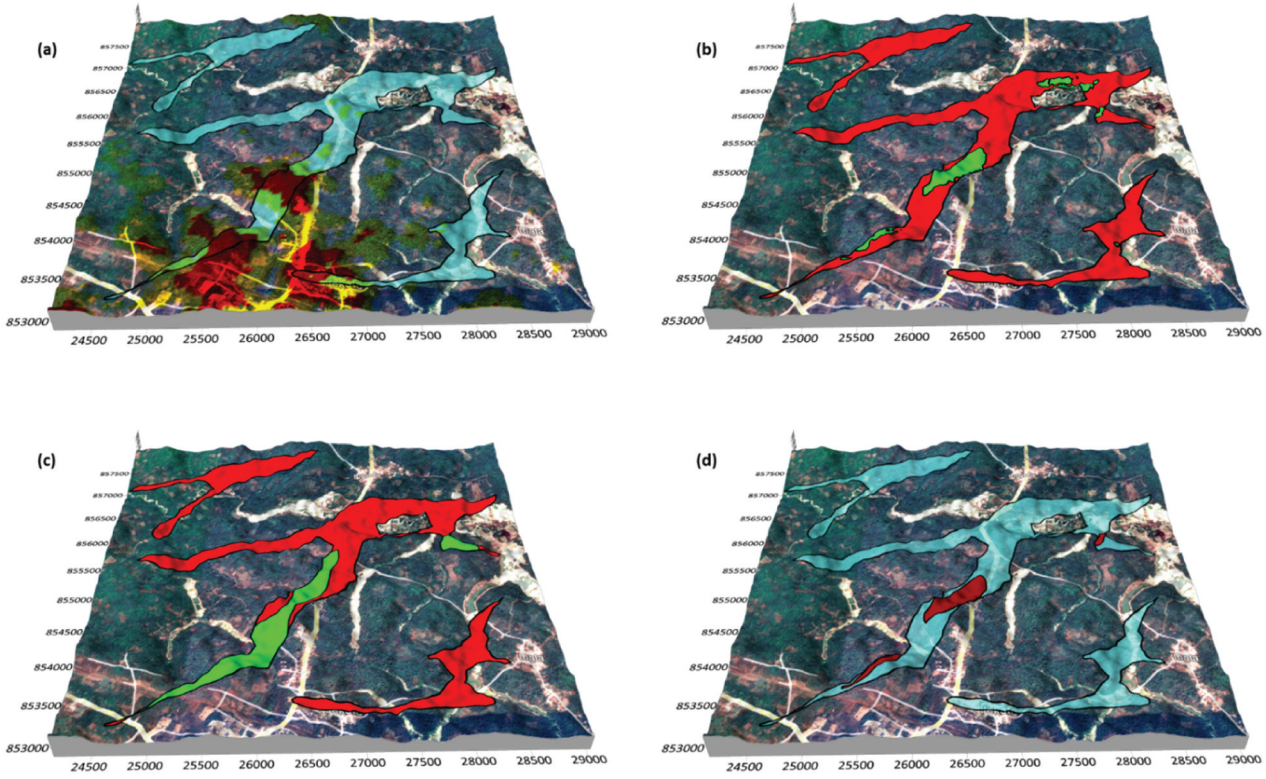

Figure 30. 3D terrain model showing (a)topographic map with elevated areas highlighted in red. (b) depth to structure areas with exhibiting depths less than 50 meters highlighted in green. (c) conductivity at 50m depths with values exceeding 2 mS/m highlighted in green (d) delineated source locations highlighted in red.

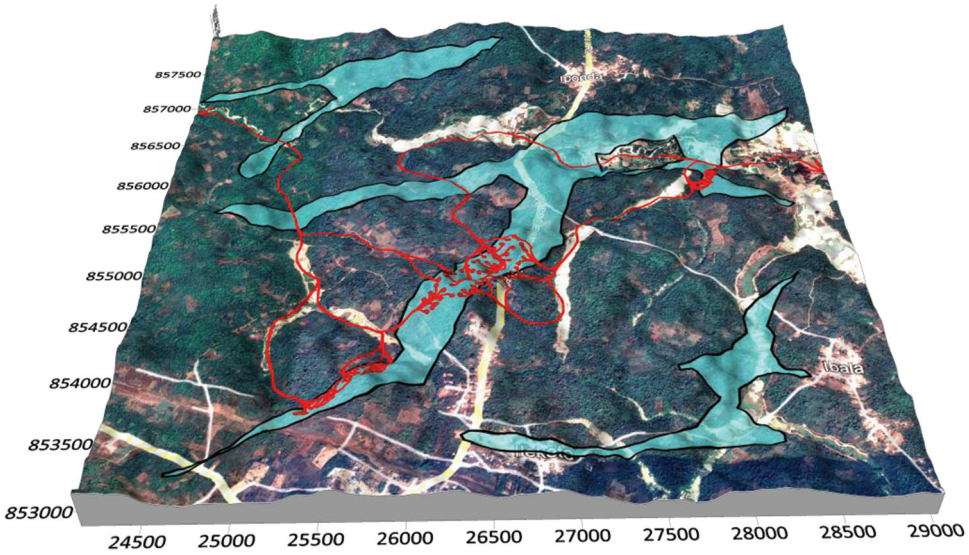

Figure 31. 3D terrain model showing (a)topographic map with elevated areas highlighted in red. (b) depth to structure areas with exhibiting depths less than 50 meters highlighted in green. (c) conductivity at 50m depths with values exceeding 2 mS/m highlighted in green (d) delineated source locations highlighted in green.

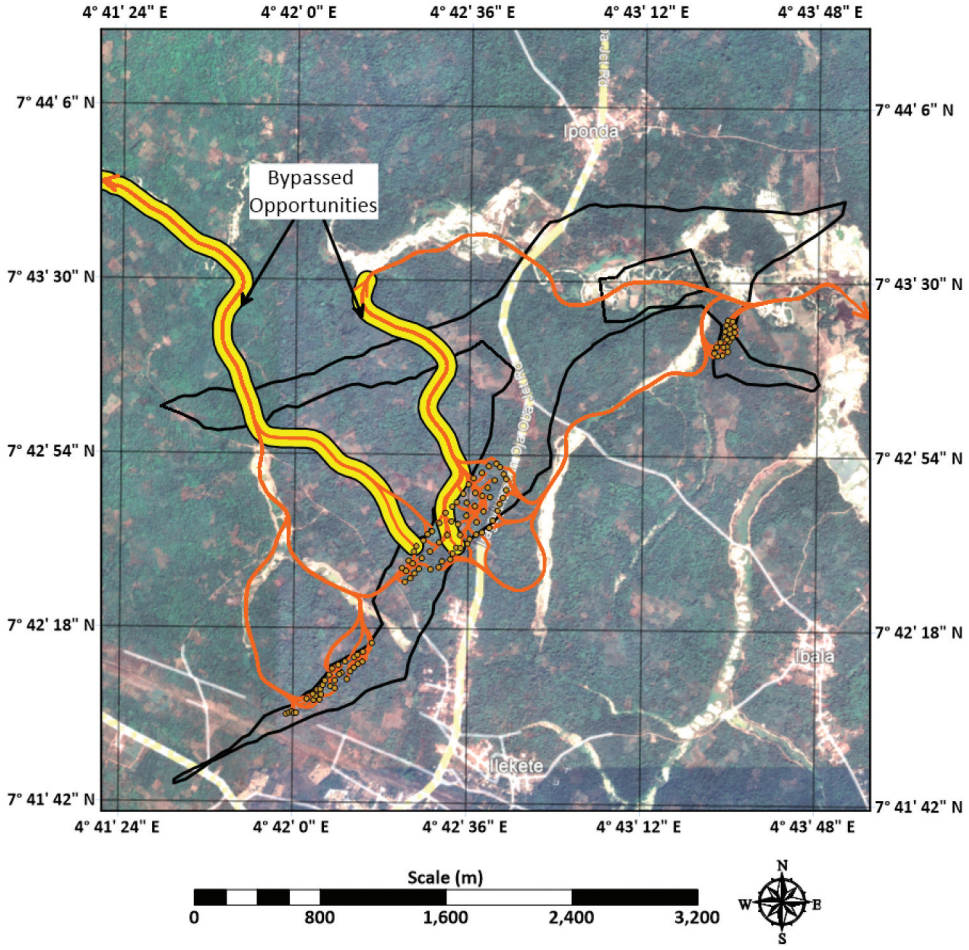

Figure 32. Base map showing conformity between the migration path of the weathered auriferous material and the alluvial gold mines. Bypassed opportunity highlighted in yellow.

out across the central fracture zone to ascertain the presence of auriferous structures within the delineated source regions (Figure 33). Additionally, an exploration trench was dug for the purpose of validating the results of the ERT and IP surveys.

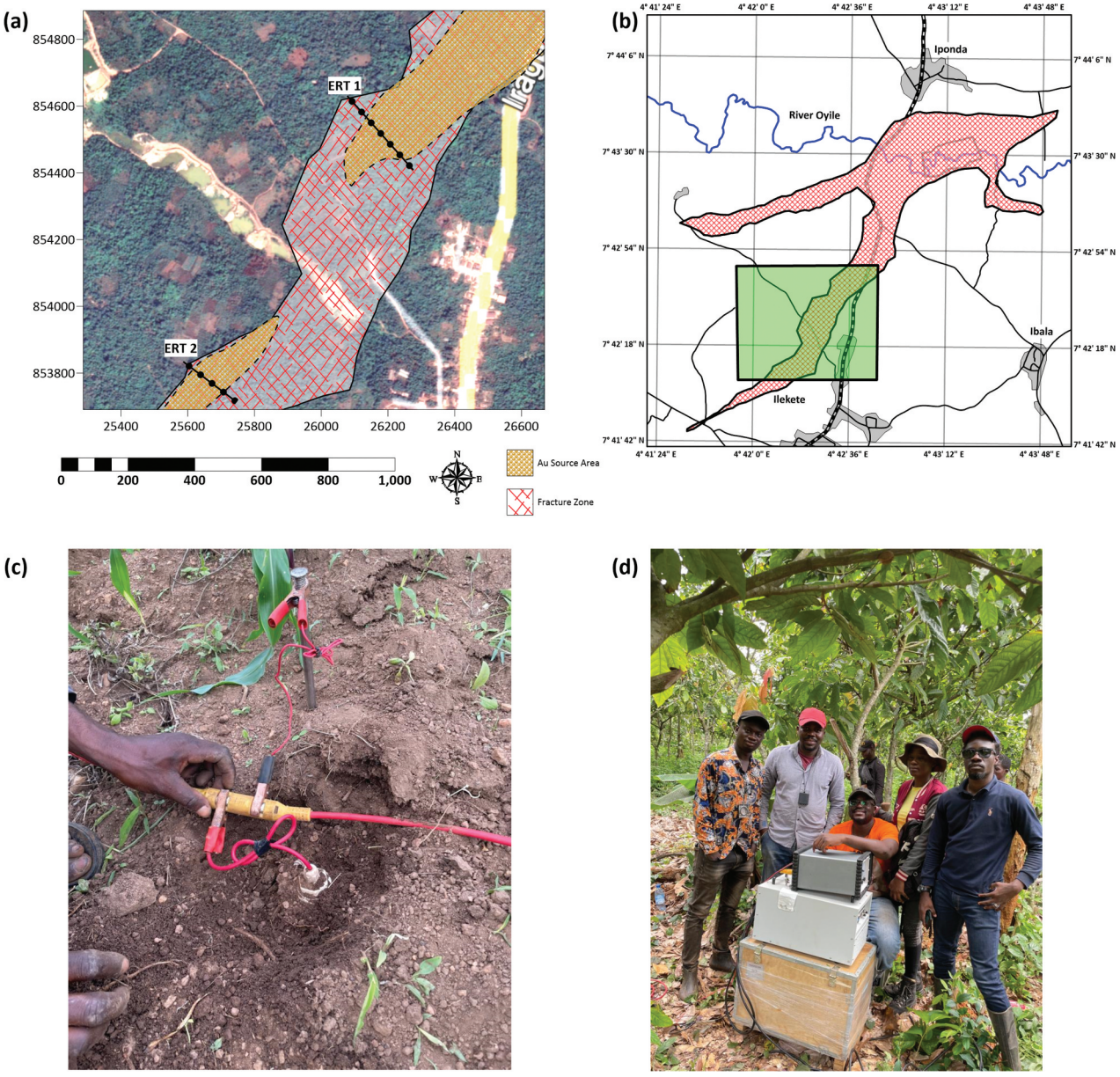

Figure 33. (a) Base map showing location of ERT survey lines. (b) map of study area showing ground truthing area. (c) stainless steel and non-polarizing electrode. (d)Earth resistivity meter

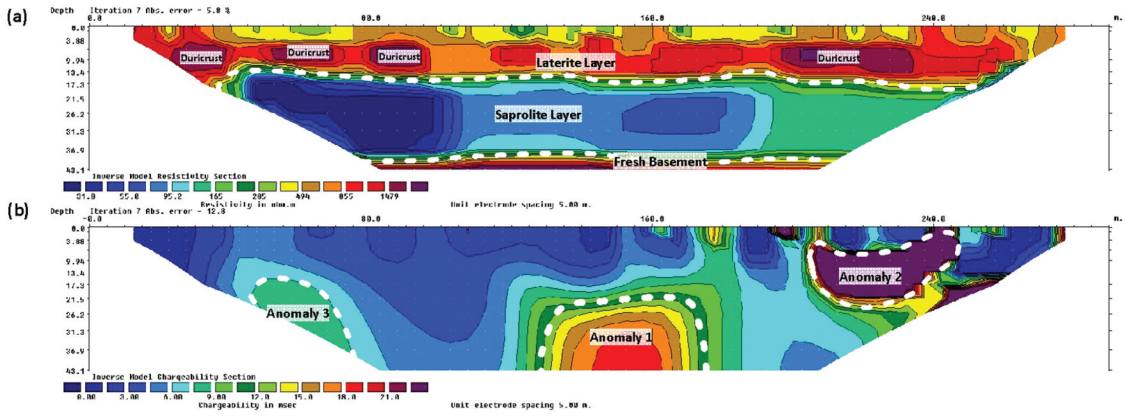

Figure 34. ERT 1(a) resistivity inversion results (b) chargeability inversion results.

5.1. Geoelectric survey results

The resistivity profiles (Figure 34 andFigure 35) identify three distinct layers: laterite, saprolite, and fresh basement. The lateritic layer is about 13 to 17 metres thick, with high resistivity anomalies suggesting the presence of hardened duricrust. The saprolite layer,

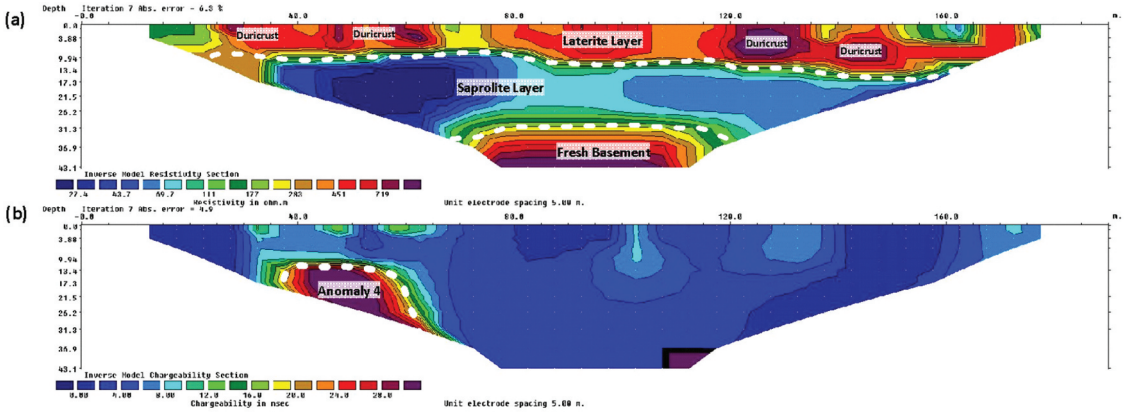

Figure 35. ERT 2(a) resistivity inversion results (b) chargeability inversion results

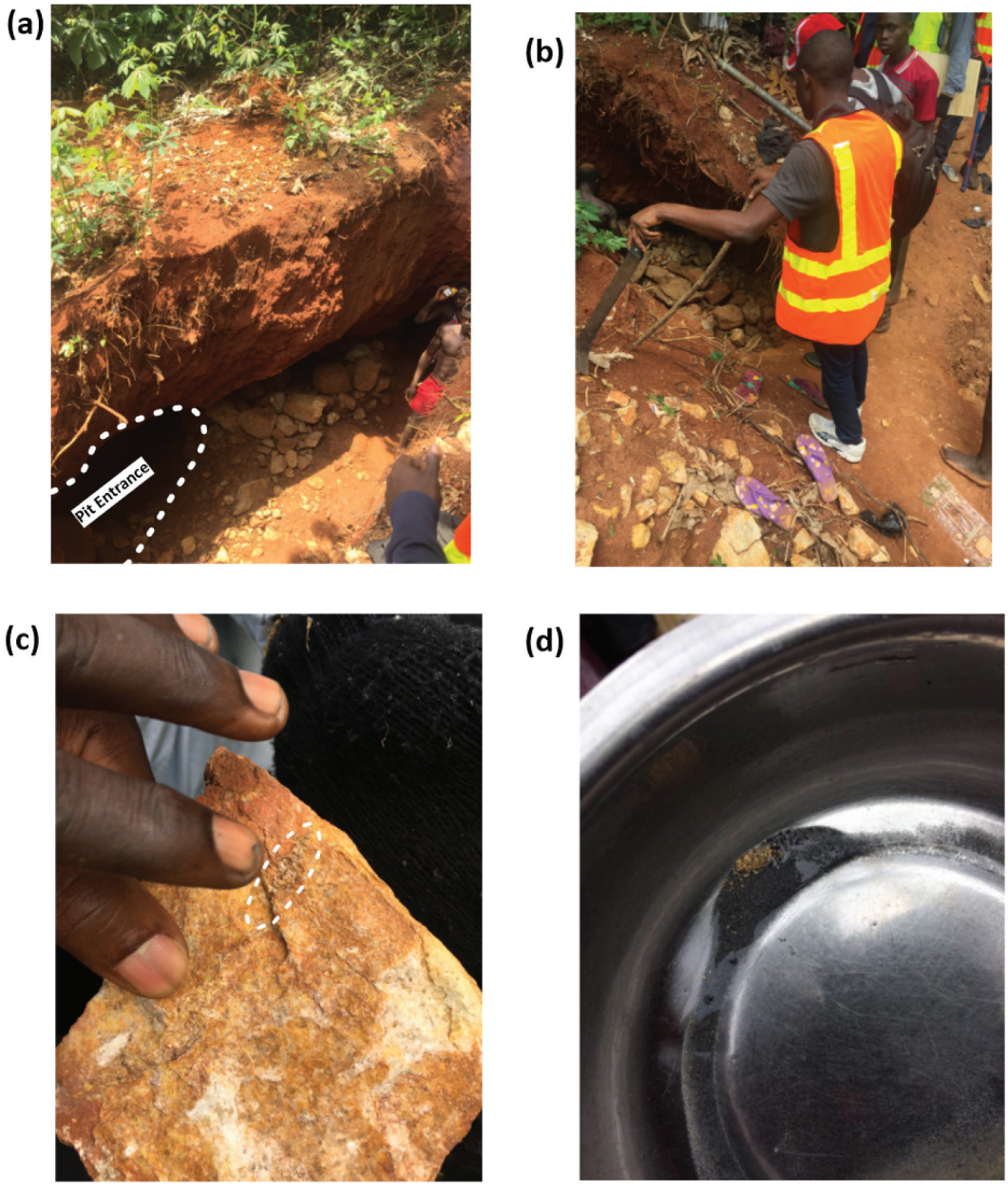

Figure 36. field photographs showing (a) trench with pit entrance (b) trench with angular quartz boulders (c) sample of quartz showing metallic particles (d) Gold particles obtained from the panning of crushed quartz boulders.

approximately 21 to 26 metres thick, exhibits low resistivity values, indicating clayey lithology. The depth to the fresh basement ranges from 35 to 43 metres, with a sharp weathering boundary in ERT 1 and a more gradual transition in ERT 2.

The chargeability sections reveal three anomalies on ERT 1 and one on ERT 2. On ERT 1 (Figure 34), Anomaly 2, with a chargeability greater than 35 msec, is interpreted as ferruginous concretions at the laterite-saprolite interface. Anomaly 1, with a chargeability around 20 msec, is considered a vertically dipping alteration zone, while Anomaly 3, with a chargeability of approximately 9 msec, is seen as a sub-vertical alteration zone. On ERT 2 (Figure 35), Anomaly 4, with a chargeability around 20 msec, is also regarded as a vertically dipping alteration zone.

These chargeability anomalies are linked to the presence of disseminated pyrite, which indicate potential auriferous structures. It is notable that the chargeability anomalies are confined to the saprolite layer, as the laterite zone, being an oxidised environment, would have converted sulphide minerals into iron oxides, which are not chargeable.

5.2. Exploration Pitting and Trenching

The locations of the chargeability anomalies were selected as targets for the exploratory trench. At ERT 1, a trench was initially dug to a depth of 4 metres targeting the chargeability anomaly 1. Then a 2- to 3-metre-wide pit was dug vertically to a depth of approximately 9 to 12 metres (Figure 36a). At this depth a large amount of dislodged angular quartz boulders are encountered. These boulders are brought to the surface by the artisanal miners and kept at the base of the trench (Figure 36b). Upon closer inspection, some of the angular quartz boulders obtained from the trench showed some yellowish metallic particles (Figure 36c). The angular quartz boulders together with saprolite materials are crushed using locally made jaw crushers. The crushed samples are then panned to recover gold (Figure 36d). The results of the panning confirmed that some of the quartz boulders are auriferous with some black metallic particles suspected to be responsible for the chargeability anomaly.

Disclosure statement

No potential conflict of interest was reported by the author(s).

References

Bafor BE. 1981. The occurrence of sulphide mineralization in the egbe area of SW Nigeria. J Min Geol 18 1. 175–179.

Bierlein FP, Craw D. 2008. Petrogenetic character and provenance of metabasalts in the aspiring and torlesse terranes, South Island, New Zealand: implications for the gold endowment of the Otago Schist? Chem Geol. 260 (3–4):301–315. doi: 10.1016/j.chemgeo.2009.01.016.

Bierlein FP, Pisarevsky S. 2008. Plume-related oceanic plateaus as a potential source of gold mineralisation. Econ Geol. 103(2):425–430. doi: 10.2113/gsecongeo.103.2.425.

Caby R, Boesse JM. 2001. Pan-African nappe system in southwest Nigeria: the ife-ilesha schist belt. J Afr Earth Sci. 33(2):211–225. doi: 10.1016/S0899-5362(01)80060-9.

Calcagno P, Chilès JP, Courrioux G, Guillen A. 2008. Geological modelling from field data and geological knowledge: part I. Modelling method coupling 3D potential-field interpolation and geological rules. Phys Of The Earth Planet Inter. 171(1–4):147–157. doi: 10.1016/j.pepi.2008.06.013.

Colvine AC 1988. *An integrated model for the origin of Archean lode-gold deposits.*(ON): Ontario Ministry of Natural Resources.

Elmer FL, White RW, Powell R. 2006. Devolatilization of metabasic rocks during greenschist–amphibolite facies metamorphism. J Metamorph Geol. 24(6):497–513. doi: 10.1111/j.1525-1314.2006.00650.x.

Elueze A. 1981. Geochemistry and petrotectonic setting of metasedimentary rocks of the schist belt of Ilesha area, S. W. Nigeria. J Min Geol 18. 194–197.

Elueze AA, Olade MA. 1985. Interpretation through factor analysis of stream-sediment reconnaissance data for gold exploration in Ilesha greenstone belt, southwest Nigeria. Appl Earth Sci 94. 155–160.

Garba I. 1988. The variety and possible origin of the Nigerian gold mineralization. J Afr Earth Sci. 7(7–-8):981–986. doi: 10.1016/0899-5362(88)90011-5.

Goldfarb JR, Leach DL, Miller ML, Pickthorn WJ. 1986. *Geology, metamorphic setting, and genetic constraints of epigenetic lode-gold mineralization within the Cretaceous Valdez Group, south-central Alaska*. s.l: Geological Association of Canada Special Paper.

Goldfarb RJ, Leach DL, Pickthorn WJ, Paterson CJ. 1988. Origin of lode–gold deposits of the Juneau gold deposit, southeast Alaska. Geology. 16(5):440–443. doi: 10.1130/0091-7613(1988)016<0440:OOLGDO>2.3.CO;2.

Hagemann SG, Lisitsin V, Huston DL. 2016. Mineral system analysis: quo vadis. Ore Geol Rev. 76:504–522. doi: 10.1016/j.oregeorev.2015.12.012.

Henley RW, Norris RJ, Paterson CJ. 1976. Multistage ore genesis in the New Zealand geosyncline: a history of post-metamorphic lode emplacement. Mineral Deposita. 11(2):180–196. doi: 10.1007/BF00204480.

Hronsky JM, Groves DI, Loucks RR, Begg GC. 2012. A unified model for gold mineralisation in accretionary orogens and implications for regional-scale exploration targeting methods. Mineralium Deposita. 47(4):339–358. doi: 10.1007/s00126-012-0402-y.

Huston DL, Mernagh TP, Hagemann SG, Doublier MP, Fiorentini M, Champion DC, Lynton Jaques A, Czarnota K, Cayley R, Skirrow R, et al. 2016. Tectono-metallogenic systems — the place of mineral systems within tectonic evolution, with an emphasis on Australian examples. Ore Geol Rev. 76:168–210. doi: 10.1016/j.oregeorev.2015.09.005.

Ige OA, Holness MB. 2002. Paragenesis, conditions and timing of the metamorphism of the metapelitic rocks in the ilesha schist belt, southwestern Nigeria. Niger Min And Geosci Soc. 38(2):71–79. doi: 10.4314/jmg.v38i2.18777.

Ige OA, Okrusch M, Schüssler U, Schmädicke E, Cook NJ. 1998. The metamorphosed mafic-ultramafic complex of Mokuro, ilesha schist belt, southwestern Nigeria. J Afr Earth Sci. 26(4):593–618. doi: 10.1016/S0899-5362(98)00035-9.

Kerrich R, Fryer BJ. 1979. Archaean precious-metal hydrothermal systems, Dome Mine, Abitibi Greenstone Belt: II. REE and oxygen isotope relations. Can J Earth Sci. 16(3):440–458. doi: 10.1139/e79-041.

Kerrich R, Fyfe WS. 1981. The gold—carbonate association: source of CO2, and CO2 fixation reactions in Archaean lode deposits. Chem Geol. 33(1–4):265–294. doi: 10.1016/0009-2541(81)90104-2.

Klemm DD, Schneider W, Wagner B. 1983. The Precambrian metavolcano-sedimentary sequence east of ife and Ilesha/sw Nigeria. A Nigerian 'greenstone belt'? J Afr Earth Sci. 2(2):161–176. doi: 10.1016/S0731-7247(84)80011-7.

Martelet G, Truffert C, Tourlière B, Ledru P, Perrin J. 2006. Classifying airborne radiometry data with agglomerative hierarchical clustering: a tool for geological mapping in context of rainforest (French Guiana). Int J Appl Earth Observation And Geoinf. 8(3):208–223. doi: 10.1016/j.jag.2005.09.003.

McCuaig CT, Beresford S, Hronsky J. 2010. Translating the mineral systems approach into an effective exploration. Ore Geol Rev. 38(3):128–138. doi: 10.1016/j.oregeorev.2010.05.008.

Nabighian MN. 1972. The analytic signal of two-dimensional magnetic bodies with polygonal cross-section: its properties and use for automated anomaly interpretation. Geophysics. 37(3):507–517. doi: 10.1190/1.1440276.

Olade MA, Elueze AA. 1979. Petrochemistry of the ilesha amphibolite and Precambrian crustal evolution in the Pan-African domain of SW Nigeria. Precambrian Res. 8(3–4):303–318. doi: 10.1016/0301-9268(79)90033-0.

Osinowo OO, Fashola OE, Ayolabi EA, Olayinka AI. 2021. Structural mapping and gold mineralisation potential evaluation from airborne time – domain electromagnetic (TDEM) data of ilesha schist belt, southwestern Nigeria. Exploration Geophysics. 53(3):237–254. doi: 10.1080/08123985.2021.1922275.

Oyawoye MO. 1964. The geology of Nigerian basement complex – a survey of our present knowledge of them. J Min Geol 1. 87–102.

Oyinloye AO. 2006. Metallogenesis of the lode gold deposits in Ilesha Area of Southwestern Nigeria. Pak J Sci And Ind Res 49. 1–11.

Oyinloye AO, Steed GM. 1996. Geology and geochemistry of the iperindo primary gold deposits ilesha schist belt Southwestern Nigeria. Inferences from stable carbon isotope studies. Afr J Sci Technol 8. 16–19.

Phillips GN, Groves DI. 1983. The nature of Archaean gold-bearing fluids as deduced from gold deposits of Western Australia. J Geological Soc Of Aust. 30(1--2):25–39. doi: 10.1080/00167618308729234.

Phillips GN, Groves DI, Brown IJ. 1987. Source requirements for the Golden Mile, Kalgoorlie: significance to the metamorphic replacement model for Archean gold deposits. Can J Earth Sci. 24(8):1643–1651. doi: 10.1139/e87-158.

Phillips GN, Powell R. 2010. Formation of gold deposits: a metamorphic devolatilization model. J Metamorph Geol. 28(6):689–718. doi: 10.1111/j.1525-1314.2010.00887.x.

Pilkington M. 2009. 3-D magnetic data-space inversion with sparseness constraints. Geophysics. 74(1):L7–L15. doi: 10.1190/1.3026538.

Powell R, Will T, Phillips G. 1991. Metamorphism in Archaean greenstone belts– calculated fluid compositions and implications for gold mineralization. J Metamorph Geol. 9(2):141–150. doi: 10.1111/j.1525-1314.1991.tb00510.x.

Rahaman MA, Ocan O. 1978. On relationship in the Precambrian migmatite-gneiss of Nigeria. J Min And Geol 15. 23–30.

Reid AB, Allsop JM, Granser H, Millett AJ, Somerton IW. 1990. Magnetic interpretation in three dimensions using Euler deconvolution. Geophysics. 55(1):80–91. doi: 10.1190/1.1442774.

Stewart I, Miller DT. 2018. Directional tilt derivatives to enhance structural trends in aeromagnetic grids. J Appl Geophysics. 159:553–563. doi: 10.1016/j.jappgeo.2018.10.004.

Thompson DT. 1982. EULDPH: a new technique for making computer-assisted depth estimates from magnetic data. Geophysics. 47(1):31–37. doi: 10.1190/1.1441278.

Tomkins AG. 2010. Windows of metamorphic sulfur liberation in the crust: implications for gold deposit genesis. Geochim Et Cosmochim Acta. 74(11):246–3259. doi: 10.1016/j.gca.2010.03.003.

Witherly K. 2015. Building effective mineral system models; the importance of merging geophysical observation with geological inference. ASEG Ext Abstr. 2015(1):1–4. doi: 10.1071/ASEG2015ab117. *ASEG Extended Abstracts*.

Wyborn LA, Heinrich CA, Jaques AL. 1994 1994 AusIMM Annual Conference 9/08/94 Darwin, Australia. 109–115 https://www.ausimm.com/publications/conference-proceedings/1994-auslmm-annual-conference-darwin-august-1994/. Melbourne, Australia: Darwin, AusIMM Publication Series.

Wyman DA, Cassidy KF, Hollings P. 2016. Orogenic gold and the mineral systems approach: resolving fact, fiction and fantasy. Ore Geol Rev. 78:322–335. doi: 10.1016/j.oregeorev.2016.04.006.